CORE
Metadata, citation and similar papers at core.ac.uk
Provided by Illinois Digital Environment for Access to Learning and Scholarship Repository

© 2013 Joseph R Bernhardt

RADIATION-ENHANCED DIFFUSION OF OXYGEN-18 IN URANIUM DIOXIDE THIN FILMS

BY

JOSEPH R BERNHARDT

THESIS

Submitted in partial fulfillment of the requirements
for the degree of Master of Science in Nuclear, Plasma, & Radiological Engineering
in the Graduate College of the
University of Illinois at Urbana-Champaign, 2013

Urbana, Illinois

Master's Committee:

Professor Brent J. Heuser, Director of Research
Professor James F. Stubbins

ABSTRACT

Anion radiation enhanced diffusion (RED) and thermal diffusion of a buried ^{18}O tracer layer in thin film UO_2 was measured using Secondary-Ion Mass Spectroscopy (SIMS). Thin films were grown using a dedicated magnetron sputtering chamber. Samples were irradiated with 1.8 MeV Kr^+ over a temperature range from 295 K to 623 K. Measurements have been made for both single crystal and textured films. This difference in crystal structure led to significantly different results. Thin film stoichiometry was also shown to have an effect on RED and thermal diffusion. For RED, activation energies found from best fit analysis were E_a = 0.83 and E_a = 0.37, for single crystal and textured samples, respectively. RED for single crystal UO_2 thin films can be represented by,

$$D_{RED} = 8.7 \times 10^{-14} \exp\left(\frac{-0.83}{\mathrm{kT}}\right) \ cm^2/sec$$

RED for textured UO_2 thin films can be represented by,

$$D_{RED} = 2.0 \times 10^{-15} \exp\left(\frac{-0.37}{\mathrm{kT}}\right) \ cm^2/sec$$

Thermal diffusion measurements resulted, from best fit analysis, in similar activation energies for single crystal and textured thin films, E_a = 0.46 and E_a = 0.53, respectively. This was shown to agree well with published experimental and calculated values for UO_{2-x} for anion vacancies. Thin films used in this work were thought to be substoichiometric and thermal diffusion is thought to be controlled by anion vacancies. Mixing parameter measurements found $\underline{\xi}$ = 2.1 ± 0.2 $Å^5 eV^{-1}$ on the anion sublattice, which indicated that ballistic mixing was the dominant mechanism of ion-mixing and that thermal spike activity is negligible.

ACKNOWLEDGEMENTS

I would first like to express my gratitude to Professor Brent Heuser for his help and guidance during my tenure at the University of Illinois. He has been instrumental in aiding my studies as both an undergraduate and graduate student. His patience and dedication towards his students is greatly appreciated, and the knowledge I have gained working with him is invaluable. I would also like to thank Professor James F. Stubbins. He has been a true role model throughout my time at the University of Illinois. He was always there if I needed guidance, whether with school or life decisions. I would also like to thank my research group, especially Xiaochun Han and Mohamed ElBakhshwan, for their guidance and support throughout.

The faculty and staff in the Nuclear Engineering department office have been extremely helpful. They have gone out of their way to make my time at the University of Illinois an enjoyable one, and for that, I am very grateful.

The staff at the Materials Research Lab (MRL) has been a great help, especially Dr. Mauro Sardelo, Dr. Timothy Spila, and Doug Jeffers.

I would also like to acknowledge the National Academy for Nuclear Training (NANT) Fellowship Program for providing me the financial support necessary to attend graduate school at the University of Illinois.

Finally I would like to thank my family and friends, especially my loving parents, for all of their love and support.

TABLE OF CONTENTS

CHAPTER 1: INTRODUCTION 1
CHAPTER 2: EXPERIMENTAL 17
CHAPTER 3: RESULTS 37
CHAPTER 4: ANALYSIS 56
CHAPTER 5: DISCUSSION 66
CHAPTER 6: SUMMARY 72
CHAPTER 7: FUTURE WORK 74
BIBLIOGRAPHY 76

CHAPTER 1: INTRODUCTION

Uranium dioxide (UO_2) is the most widely used fuel material in commercial nuclear reactors. Due to this it is vital to have a thorough understanding of UO_2 properties. Mass transport in urania is dominated by diffusion processes on the anion sublattice near stoichiometric composition [1, 2]. Many oxygen diffusivity in urania studies have been undertaken in the 1960s, 70s, and 80s (see for instance [3, 4, 5]). However, radiation enhanced diffusion (RED) studies in UO_2 are not common in published literature. Additionally, there exists no experimental data of anion RED in urania, and only one known cation RED experiment in urania has been published [6]. The aim of this study will be to analyze both thermal and radiation transport properties of oxygen in UO_2. These transport properties, whether thermally or radiation induced, affect in-reactor operation performance and long-term storage.

The aim of this study is to measure the anionic diffusivity of ^{18}O in thin film UO_2. A dedicated magnetron sputtering facility [18] has been used to grow thin films of uranium dioxide on yttria-stabilized zirconia (YSZ) substrates, with a tracer layer of ^{18}O at the film midplane. X-ray diffraction (XRD) and x-ray photoelectron spectroscopy (XPS) have been used to characterize the as-grown thin films. Secondary-Ion Mass Spectroscopy (SIMS) has been used to measure relative composition depth profiles before and after both thermal and irradiation treatments. Thin films have been exposed to heavy-ion bombardment with 1.8 MeV Kr^+, at both room temperature and elevated temperature. At elevated temperature, thermal diffusivity measurements have also been quantified. Diffusivity will be measured by analyzing SIMS profiles of ^{18}O tracer layers. A Gaussian profile has been fit to each ^{18}O peak and then converted to diffusivity. This has been done to study both thermal and radiation transport properties. Irradiation has been done at room temperature, to measure the mixing parameter, and at elevated

temperature to measure RED and thermal diffusivities. This study aims to increase knowledge of light water reactor (LWR) fuel performance, in both normal operating conditions and transient scenarios, and aims to aid in existing modeling efforts of both mass and heat transport in urania.

In Section 1.1 to follow, background is presented for both RED and the mixing parameter. Section 1.2 presents a thorough review of literature on diffusion processes in UO_2, including anionic diffusion and RED. The experimental procedures are outlined in Chapter 2. Sample fabrication and analysis techniques such as x-ray diffraction (XRD), secondary-ion mass spectroscopy (SIMS), and the irradiation experiments are included in Chapter 2. Chapter 3 is a presentation of the experimental results. Chapter 4 contains a detailed analysis and discussion of all results and findings. Finally, Chapter 5 is a summary of the information gained from this work.

1.1 Background Information

1.1.1 Theory of Radiation Enhanced Diffusion (RED)

Diffusion in solids occurs due to defects in the crystal, either vacancies or interstitials. Radiation enhanced diffusion is a diffusion process in which these defect species are created in excess of equilibrium when exposed to energetic heavy-ions at elevated temperatures. Vacancies and interstitials are created at a constant rate and result in a concentration larger than the equilibrium concentration. Radiation can increase the rate of diffusion by increasing the concentration of defect species (e.g. vacancies) or by creating diffusion channels which are not available during thermally activated processes (e.g. interstitials and di-vacancies) [8, 9].

The first fundamental aspects of RED theory for metals were presented by Lomer [10], Dienes and Damask [9] and later reviewed by Sizmann [8]. The equation for the total diffusion coefficient for a particular lattice atom, D_a, is given by,

$$D_a = f_v D_v C_v + f_i D_i C_i + f_{2v} D_{2v} C_{2v} + \ldots \quad (1.1)$$

where *f* are correlation factors (usually < 1) [11], D are diffusion coefficients, and C are concentrations. Subscript *v* stands for vacancies, *i* stands for interstitials, 2*v* stands for di-vacancies. As stated previously and seen in equation (1.1), the diffusion coefficient of a lattice atom will increase if defect concentrations (e.g. C_v) increase, or if additional diffusion channels are created (e.g. D_{2v}).

A model for diffusion kinetics is constructed through the use of chemical rate equations. This can be written in two simultaneous and consecutive rate equations, namely,

$$\frac{dC_v}{dt} = K_0 - K_{iv} C_i C_v - K_{vs} C_v C_s \quad (1.2)$$

$$\frac{dC_i}{dt} = K_0 - K_{iv} C_i C_v - K_{is} C_i C_s \quad (1.3)$$

where C_v, C_i, and C_s are the vacancy, interstitial, and sink concentrations respectively. K_0 is the Frenkel pair production rate. K_{iv}, K_{vs}, and K_{is} are the interstitial-vacancy recombination rate coefficient, vacancy-sink reaction rate coefficient, and interstitial-sink reaction rate coefficient respectively. For these equations to be valid it is assumed that Frenkel pair production is homogeneous, sinks for v and i are equal, higher order terms such as di-vancancies are ignored, and no concentration gradients of defects are present.

For the case of vacancy-interstitial recombination and point defect annihilation at a spherical sink, the rate constants become [8],

$$K_{iv} = 4\pi r_{iv}(D_i + D_v)/\Omega \quad (1.4)$$

$$K_{is} = 4\pi r_{is} D_i/\Omega \quad (1.5)$$

$$K_{vs} = 4\pi r_{vs} D_v/\Omega \quad (1.6)$$

where, r_{ij} are the reaction radii between species, and Ω is the atomic volume. Steady-state solutions for the vacancy and interstitial concentrations have been determined to be [8],

$$C_v^{(s)} = -\frac{K_{is}C_s}{2K_{iv}} + \left[\frac{K_0 K_{is}}{K_{iv}K_{vs}} + \frac{K_{is}^2 C_s^2}{4K_{iv}^2}\right]^{1/2} \quad (1.7)$$

$$C_i^{(s)} = -\frac{K_{vs}C_s}{2K_{iv}} + \left[\frac{K_0 K_{vs}}{K_{iv}K_{is}} + \frac{K_{vs}^2 C_s^2}{4K_{iv}^2}\right]^{1/2} \quad (1.8)$$

For steady-state $\left(\frac{dC}{dt} = 0\right)$, the radiation enhanced diffusion coefficient can be written as,

$$D_{RED} = D_v C_v + D_i C_i \quad (1.9)$$

However, with the assumption of symmetry (i.e. $C_i = C_v$) in both C_i and C_v this can be rewritten as,

$$D_{RED} = 2D_v C_v \quad (1.10)$$

1.1.2 Mixing Parameter

As an incident ion penetrates a solid, it deposits energy to both the atoms and electrons of the solid. Target atoms in the solid can be displaced by several lattice sites. If this process takes place near a boundary separating two different materials (e.g. film material and substrate material) interface mixing occurs. In general, ion-beam mixing can occur in one of three displacement processes, which are the following: direct recoil displacement, collision cascades, and thermal spikes [12]. In the case of 1-D transport, the total mean square displacement $\langle x^2 \rangle$ [cm^2] is proportional to the product of the diffusion coefficient D [cm^2/sec] and the irradiation time t [sec], as seen in the following equation,

$$\langle x^2 \rangle \propto Dt = 2Dt \quad (1.11)$$

The total mean square displacement can also be expressed as,

$$\langle x^2 \rangle = (\sigma_{irr})^2 - \left(\sigma_{ref}\right)^2 \quad (1.12)$$

where, σ_{irr} and σ_{ref} are standard deviations of the Gaussian distributions of the tracer material (^{18}O here) for the irradiated and unirradiated cases, respectively. This product is also proportional to the product of the ion fluence Φ [ions/cm^2] and the nuclear differential energy deposited F_D [eV/cm/ion], which can be expressed in the following way,

$$Dt = \xi \Phi F_D \quad (1.13)$$

where the constant of proportionality is known as the mixing parameter, ξ [cm^5/eV]. The mixing parameter is a measure of ballistic mixing during irradiation, which from equation 1.13 is given by,

$$\xi = \frac{Dt}{\Phi F_D} \quad (1.14)$$

The mixing parameter is a constant of proportionality between the total nuclear differential energy deposited and the total mean square displacement $\langle x^2 \rangle$ induced by cascade damage.

Therefore, the mixing parameter characterizes transport associated with displacement cascades, and directly shows the effects of the type of irradiation particle, specimen temperature, and ion flux [7, 12]. These typically are measured at room temperature to avoid long-range transport associated with elevated temperature. In 1998, Sambeek and Averback made calculations of the mixing parameter on both anion and cation sublattices [12]. These authors grew thin films of MgO, using molecular beam epitaxy (MBE), with buried tracer layers of ^{18}O to study diffusion on the anion sublattice and buried tracer layers of Ca and Zn to study diffusion on the cation sublattice. To measure the mixing parameter irradiation was performed, at 303 K, using 2.0 MeV Kr^+ and 1.0 MeV Ne^+ (anion) and 2.0 MeV Kr^+ (cation). Data from these measurements yielded ξ = 2-5 $Å^5 eV^{-1}$ for the anion sublattice and ξ = 1-3 $Å^5 eV^{-1}$ for the cation sublattice, which is indicative of ballistic mixing and relatively independent of the material [12]. Low values, which are generally taken to be values less than 5 $Å^5 eV^{-1}$, indicate ballistic mixing is the dominant form of ion-mixing and thermal-spike mixing is negligible. Thermal-spike mixing refers to the local atomic transport that may occur when a crystal lattice is heated locally after the ballistic phase of a displacement cascade [21]. Thermal spike mixing in MgO is small since MgO has a high melting point and Mg and O have small atomic numbers [12].

1.2 Literature Review

1.2.1 Anion Diffusion in UO_2

Knowledge of transport phenomena is of vital importance in understanding the behavior of uranium dioxide. These transport properties, whether they are thermally or radiation induced, affect performance in many areas such as: in-reactor operation and long-term storage conditions. Studying these transport phenomena increase knowledge of light water reactor (LWR) fuel performance, in both normal operating conditions and transient scenarios, and will aid in existing modeling efforts of both mass and heat transport in urania.

Uranium dioxide consists of a fluorite crystal structure, as shown in Figure 1.1. Uranium atoms are arranged on a face centered cubic (FCC) lattice, with oxygen atoms arranged in a simple cubic lattice on the tetrahedral sites of the cation FCC lattice. Each standard unit cell consists of eight uranium atoms and four oxygen atoms. UO_2 has a lattice parameter $a_0 = 5.470$ Å. This structure is considered to be an open structure, which can accommodate additional oxygen atoms at interstitial sites. Additionally, this structure can undergo a valence change from U^{4+} to U^{+5}. These two factors give rise to its propensity to allow for anionic mobility within its structure and stability up to $UO_{2.3}$. However, hypostoichiometric uranium dioxide is difficult to achieve, and is only measureable at high temperatures [13].

A number of studies characterizing the thermal diffusivity of oxygen through urania have been carried out. One of the first self-diffusion of oxygen studies was carried out by Auskern and Belle in 1961 [3]. Using the isotopic exchange reaction of carbon dioxide enriched in ^{18}O and uranium dioxide powders, the self-diffusion of oxygen was studied in stoichiometric and non-stoichiometric UO_2. Isotopes of oxygen were exchanged at the interface of the solid and gas

phases. Experiments were carried out in temperatures ranging from 823-1053 K. In stoichiometric UO_2, diffusion of oxygen was found to be represented by,

$$D = 1.2 \times 10^3 \exp(-2.83/kT) \ [cm^2/sec] \quad (1.15)$$

Increasing the oxygen content slightly in UO_{2+x}, from x = 0.004 to x = 0.063, was shown to greatly increase the diffusion coefficient and reduce the activation energy by a factor of two. The authors concluded that the diffusion current carrier was interstitial oxygen, since self-diffusion rates depended strongly on the amount of oxygen interstitials. Results were shown to be consistent with the interstitialcy mechanism for UO_{2+x}.

Marin and Contamin studied both uranium and oxygen self-diffusion in UO_2 [4]. Oxygen self-diffusion was studied with the use of mass spectrometry to detect the, proton ^{18}O (p, α) ^{15}N reaction product. Samples were bombarded with 665 keV protons, and ^{18}O concentrations were measured from ^{15}N profiles. In stoichiometric UO_2 at temperatures ranging from 1053-1523 K, diffusion of oxygen was found to be represented by,

$$D = 0.26 \exp(-2.57/kT) \ [cm^2/sec] \quad (1.16)$$

Three additional hyperstoichiometric UO_{2+x} compositions were studied, with x = 0.022, 0.124, and 0.167. At small deviations from the stoichiometric composition, the diffusion coefficient was shown to dramatically increase, as expressed in the following empirical equation,

$$D = 0.02016\left(x + [x^2 + 500\exp(-1.77/kT]^{\frac{1}{2}}\right)\exp(-1.52/kT) \ [cm^2/sec] \ (1.17)$$

In 1969, Belle reviewed oxygen and uranium self-diffusion in both stoichiometric and hyperstoichiometric uranium dioxide. The oxidation of UO_2 is equivalent to the introduction of U^{+5} and U^{+6} ions in the cation positions with the excess charge compensated by interstitial oxygen [14]. Therefore, in the UO_{2+x} structure the main defect is oxygen ions in interstitial positions. At this point both gas-solid isotopic exchange and the diffusion couple sectioning

technique were employed to directly measure diffusion coefficients using ^{18}O. Most measurements were conducted with ^{18}O in the gas phase. The following expression was determined for the diffusion coefficient of oxygen in stoichiometric UO_2,

$$D = 1.15 \exp(-2.46/kT) \ [cm^2/sec] \quad (1.18)$$

Diffusion constants were shown to increase, while activation energies were shown to decrease with increasing oxygen content. Thorn and Winslow produced a series of papers that suggest at elevated temperatures, diffusion coefficients in UO_{2+x} tend toward stoichiometric UO_2 in an asymptotic matter. The authors also pointed out that in UO_{2+x} systems it is critical to know the exact value of x.

Kim and Olander studied oxygen diffusion in the substoichiometric UO_{2-x} system [5]. A solid-solid diffusion couple was employed using two uranium wafers, one enriched with ^{18}O, bonded together with liquid uranium. Diffusion measurements were made using ion microprobe analysis. Diffusion coefficients were determined to be,

$$D = 4.4 \times 10^{-4} \left(\frac{x}{2}\right)\left(1 - \frac{x}{2}\right) \exp\left(-0.507/kT\right) \ [cm^2/sec] \quad (1.19)$$

where x is the deviation from stoichiometry in the UO_{2-x} system. These diffusion coefficients were shown to be almost two orders of magnitude higher than stoichiometric UO_2. Anionic vacancies were shown to be the dominant defect contributing to transport. The authors also determined that both vacancies and interstitials contribute to oxygen diffusion in stoichiometric UO_2.

In 1987, Murch and Catlow reviewed oxygen diffusion studies in UO_2, ThO_2, and PuO_2 systems [13]. In 1987, uranium dioxide had been extensively studied with approximately thirty papers published, approximately half devoted to oxygen diffusion.

In the 2000s, several papers were published studying oxygen diffusion in UO_2 using more advanced techniques. These current efforts mainly involve the use of advanced computational techniques. Two such examples are by Dorado, *et al.* [15] and Gupta, *et al.* [16]. These are fist-principles calculations and experimental studies of oxygen diffusion in uranium dioxide. However, Dorado used both approaches to describe transport phenomena in UO_2; using a solid-gas isotopic exchange at the surface of samples and ^{18}O as a tracer, oxygen diffusion coefficients were measured for both single-crystal and polycrystalline UO_2. SIMS was used to characterize the diffusion of the ^{18}O. At temperatures ranging from 1223 to 1023 K, the diffusion coefficient ranged from 10^{-10} to 10^{-13} cm^2/sec for single crystal UO_2 and 10^{-11} to 10^{-14} cm^2/sec for polycrystalline UO_2. Using density functional theory (DFT) calculations, the activation energy was calculated to be 3.2 eV and 3.3 eV for single crystal and polycrystalline UO_2, respectively [15]. Advanced computational techniques currently dominated research studies, due to the difficulty in quantifying transport in urania experimentally.

Figure 1.2 displays experimental data for oxygen diffusivities in UO_2, as discussed above. These equations have been plotted over the temperature range discussed in each respective paper.

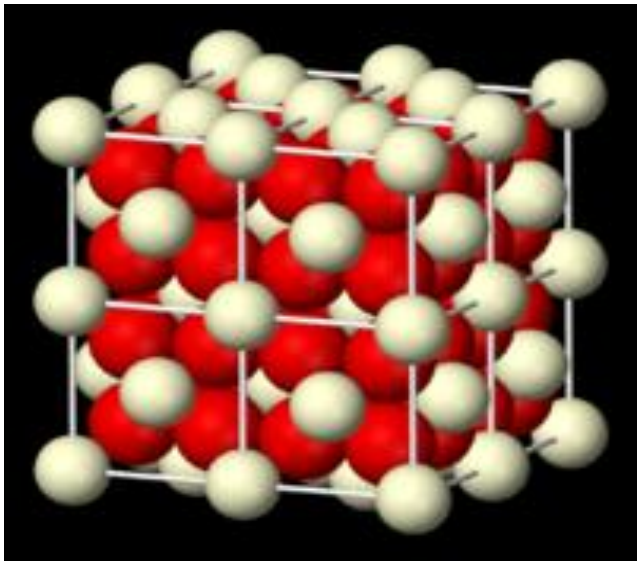

Figure 1.1: Fluorite crystal structure of UO_2. This displays a unit cell of UO_2, uranium atoms (cations) are shown in white and oxygen atoms (anions) are shown in red.

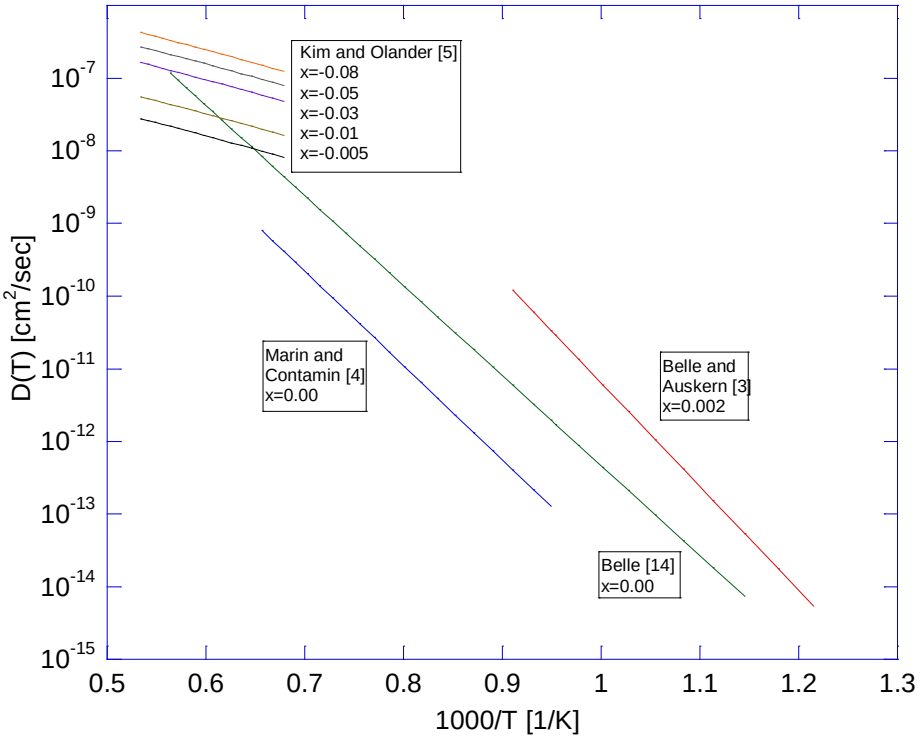

Figure 1.2: Plot of various oxygen diffusivities in UO_2. These equations have been plotted over the temperature range discussed in each respective paper. Oxygen diffusivities for Belle and Auskern, Marin and Contamin, and Belle were measured at stoichiometric composition, with x values listed above. Oxygen diffusivities for Kim and Olander were measured at substoichiometric composition, with x values listed above.

Table 1.1: Reported diffusion coefficients and activation enthalpies.

Source	Structure	|x|	D_0 [cm^2/sec]	E_a [eV]
Auskern and Belle[3]	UO_{2+x}	0.002	1.20×10^{3}	2.83
		0.004	7.0×10^{-6}	1.29
		0.063	2.06×10^{-3}	1.29
Marin and Contamin[4]	$UO_{2.00}$	0.00	0.26	2.57
Belle[14]	$UO_{2.00}$	0.00	1.15	2.46
Kim and Olander[5]	UO_{2-x}	0.005	0.11×10^{-5}	0.507
		0.01	0.22×10^{-5}	0.507
		0.03	0.65×10^{-5}	0.507
		0.05	1.07×10^{-5}	0.507
		0.08	1.68×10^{-5}	0.507
Dorado *et al.*[15]	$UO_{2.00}$	0.00	--	3.2

1.2.2 Radiation Enhanced Diffusion (RED)

As energetic heavy-ions bombard a material, defect populations are increased over that of the thermal equilibrium. In 1954, Lomer presented solutions for steady-state conditions and for the kinetics of defect build-up under irradiation for chemical rate equations, which was presented in Section 1.1.1 [10].

A simple theory of RED in solids was worked out by Dienes and Damask in 1958 [9]. For their study, alpha-brass was chosen because it is a relatively simple system. Vacancies and interstitials are created at equal rates during irradiation. Steady-state conditions occur at increasing temperatures, when vacancies and interstitials become mobile and can recombine or annihilate at sinks. This steady-state assumption is critical to the validity of the theory presented here. The authors presented several annealing mechanisms separately, namely: linear annealing of defects, annealing of defects by direct recombination, and linear annealing plus recombination. Linear annealing of defects assumes that point defects disappear by migrating to fixed sinks, such as dislocations, internal interfaces, or external free surfaces. The second case is the direct combination of vacancies and interstitials. Experimental data produced for alpha-brass agree with the theoretical model. At lower temperatures RED can dominate. Additionally, RED can become temperature independent at low temperatures (273 to 423 K for alpha-brass) [9]. The authors found that this was because linear annealing dominated in this region, since recombination would introduce a temperature dependence.

In 1968, Sizmann reviewed the effect of radiation upon the diffusion of metals, namely diffusion due to point defects in lattice structure [8]. This work expanded on work done by Lomer, and Dienes and Damask. Homogeneous systems and systems with extended sinks were studied in detail. Kinetic equations and rate coefficients were determined for these systems.

Basic solutions of chemical rate equations were given. Four main cases were analyzed: low temperatures and low sink density, low temperature and intermediate sink density, low temperature and high sink density, and high temperature.

Experimental quantification of RED in uranium dioxide is very limited in published literature. One study was done by Hoh and Matzke in 1973 [6]. The authors measured in-pile self-diffusion of uranium in stoichiometric UO_2 sinters, with a thin layer of ^{233}U used as tracer material. Measurements were performed at 1173 K, with a fission rate of 10^{13} fissions/cm^3-sec. The diffusion coefficient was found to be 1.5×10^{-16} cm^2-sec^{-1} for UO_2, which is a factor of 10^3 to 10^4 higher than the diffusion coefficient for cation thermal diffusion.

In 1998, Sambeek and Averback made measurements of RED in an oxide system, on both the anion and cation sublattice [12]. MgO thin films were grown by molecular beam epitaxy (MBE), with buried tracer layers of ^{18}O, Ca and Zn. Samples were irradiated at temperatures ranging from 303-1773 K, by 2.0 MeV Kr+ and 1.0 MeV Ne^+, He^+, and H^+. SIMS depth profiles before and after irradiation were done to measure effective diffusion coefficients of the tracer atoms. The RED of MgO was studied with a simple model to classify three distinct regimes of kinetic behavior. The highest temperature region, 1623-1773 K, was characterized by recombination-limited kinetics. In this region, the radiation enhanced diffusion coefficient for ^{18}O was found to be proportional to the square root of the irradiation flux, and the activation enthalpy was found to be 1.2 eV, which is approximately one-half the predicted migration enthalpy of anion vacancies in MgO (see references within). The intermediate region, 1373-1623 K, was shown to be a transition from recombination-limited kinetics to sink-limited kinetics. This region was shown to have a high activation enthalpy of 4.1 eV, which the authors attributed to the temperature dependence of free migrating defects. The low-temperature region,

1173-1373 K, was characterized by sink-limited kinetics. The mixing parameter was measured, at 303 K, using 2.0 MeV Kr^+ and 1.0 MeV Ne^+ for the anion sublattice and 2.0 MeV Kr^+ for the cation sublattice. Data from these measurements predict ξ to be 2-5 $Å^5 eV^{-1}$ for the anion sublattice and 1-3 $Å^5 eV^{-1}$, which is relatively independent of the material [12]. These low values indicate ballistic mixing is the dominant form of ion-mixing and thermal-spike mixing is negligible. Thermal spike mixing in MgO is small since MgO has a high melting point and Mg and O have small atomic numbers [12].

In 2010, Pappas, Heuser, and Strahle measured RED of La in single crystal, thin film CeO_2 [7]. Cerium dioxide was chosen for analysis because it is a nuclear fuel surrogate for UO_2. Cerium dioxide has the same fluorite structure and is found in the same +4 valence state with similar ionic radius. Lanthanum was chosen as an attractive surrogate for americium. Thin films of CeO_2 were grown on a sapphire substrate using MBE. X-ray diffraction analysis was performed for both as-grown and post-irradiated samples. SIMS was used to measure depth profiles of the buried tracer layers of La. Energetic heavy-ion bombardment was performed with 1.8 MeV Kr^+ ions. Room temperature experiments were performed at doses from zero to 2×10^{20} ions/m^2, as well as a constant fluence of 1×10^{20} ions/m^2 where the temperature was varied from 673 to 1206 K. Below ~800 K behavior was dominated by recombination-limited kinetics, and the cation migration energy was found to be ~0.4 eV. The activation enthalpy for La over a range 873-1073 K was found to be ~1.4 eV. The value for the mixing parameter was found to be 3.6 $Å^5 eV^{-1}$, indicative of ballistic mixing and a value similar to that found by Sambeek and Averback.

Martin *et al*., have performed a molecular dynamics (MD) study of radiation induced diffusion (RID) in uranium dioxide [17]. Simulations were performed using uranium primary

knock-on atoms between 1 and 80 keV at temperatures ranging from 300-1400 K. The total mean square displacement was shown to be roughly proportional to the number of cascade overlaps and to the energy of the primary knock-on atom (PKA). The number of displaced atoms also increases with increasing PKA energy. In simulated reactor operating conditions, the estimated uranium diffusion coefficient lies two to three orders of magnitude below those calculated experimentally under comparable conditions. The authors concluded that it is probable nuclear collisions and the associated ballistic mixing do not account for the observed atom movement in normal reactor conditions.

Presently, there exists no experimental data of anion RED in UO_2. In this study, we will attempt to study RED of oxygen through thin film UO_2. This will be accomplished using ^{18}O as a buried tracer.

CHAPTER 2: EXPERIMENTAL

2.1 Overview of Sputtering System

Sputtering is a physical vapor deposition (PVD) process that is used to grow thin films and overlayers. Sputtering is accomplished by bombarding a solid target with energetic ions, which eject atoms from the target surface due to the transfer of momentum. Ejected particles then condense and coat the substrate material. Films grown for the use in this analysis were grown using a dedicated reactive-gas magnetron sputtering system. In this sputtering system, the sputtered atoms react with the sputter gas, in the surrounding environment, to form deposited compounds. This technique employs the use of a magnetic field to confine electrons to a path above the target. The target material acts as a cathode, which emits electrons from its surface. This creates a negative potential to the positive charges in the plasma, accelerating positive ions to sputter the target. The sputtered ions form compounds with the reactive gas (oxygen) within the chamber and are deposited on the substrate material. The target can become poisoned with an oxide layer on its surface. Before growth the target is "sputter cleaned." Igniting the target for 20 minutes without the flow of oxygen removes the contamination on the surface. The sputtering system used in this work is a dedicated magnetron sputtering chamber, which consists of two chambers, a main chamber and a load lock. Figures 2.1 and 2.2 are a photograph and a schematic diagram of the magnetron sputtering system, respectively.

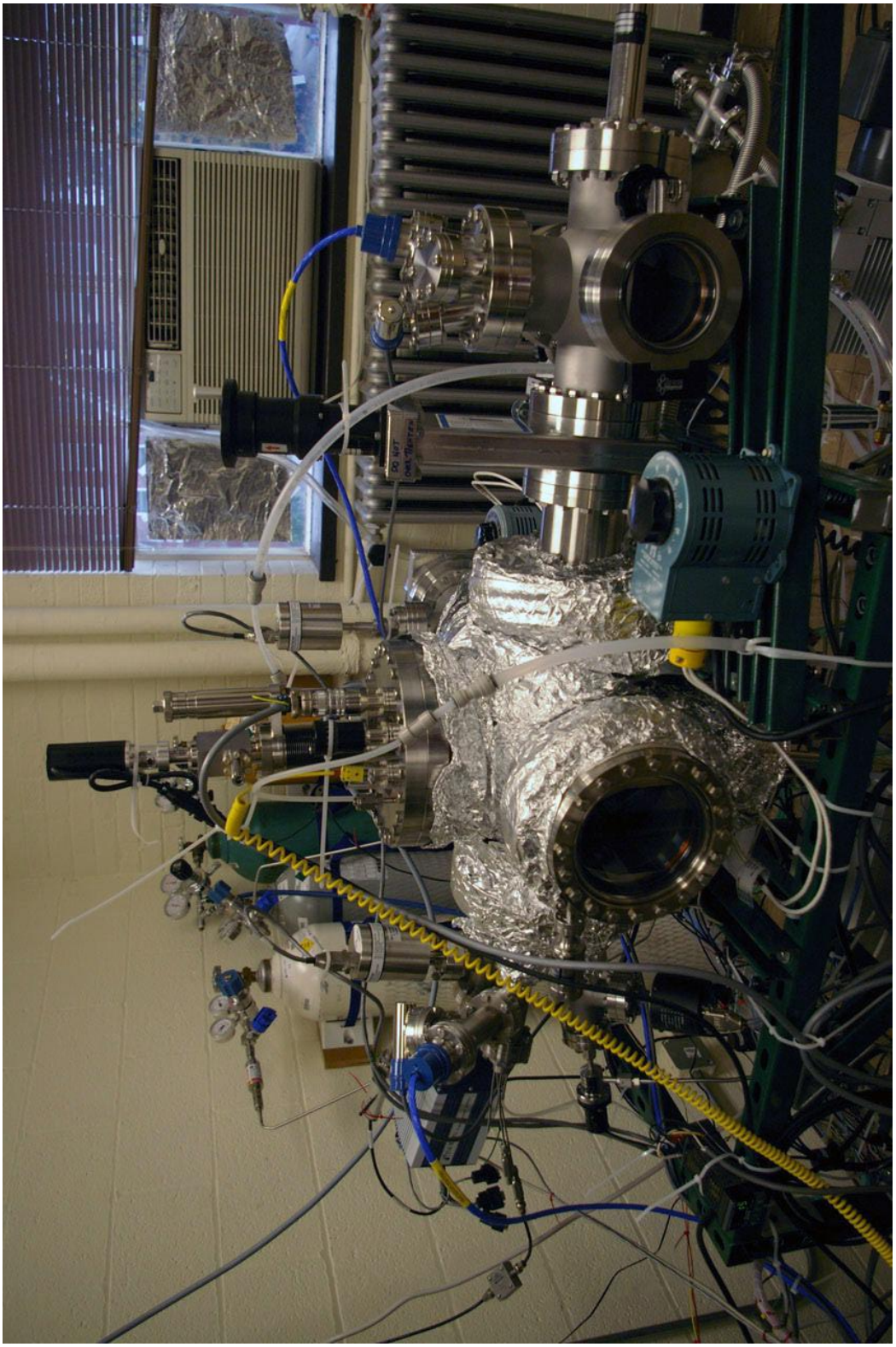

Figure 2.1: Photograph of the dedicated magnetron sputtering chamber used in this analysis.

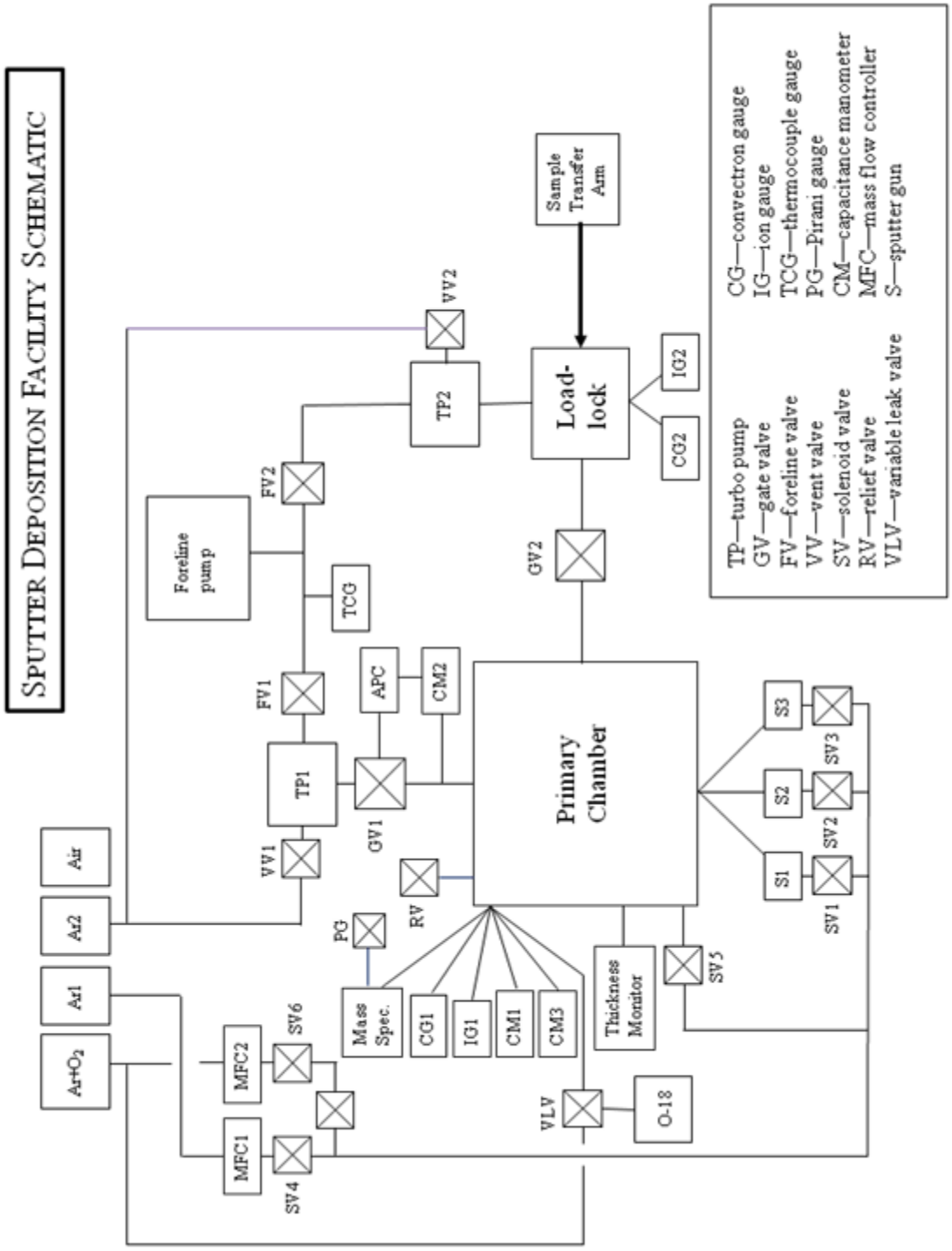

Figure 2.2: Schematic diagram of the dedicated magnetron sputtering chamber used in this analysis.

2.2 Substrate Preparation

The substrate is rigorously cleaned, using an ultrasonic bath. A small amount of trichloroethylene (TCE) is placed in a clean glass beaker, which is placed in the bath for approximately three minutes. This process is then repeated using several cleaning agents, in the following order: acetone, isopropyl alcohol (IPA), methanol, and deionized water. After the cleaning process, the substrate is mounted to an Inconel plate using silver paste and allowed to cure overnight. Figure 2.3 shows two substrates on an Inconel plate. The plate is then cured for an additional three hours, 473 K for one hour, temperature increased slowly to 673 K over one hour, and 673 K for one hour. After cooling, the plate is placed in the load lock and evacuated to a pressure of approximately 1×10^{-6} T. A transfer rod is used to relocate the plate into the main chamber. The system is pumped overnight to achieve a pressure of approximately 1×10^{-8} T. Sample stage rotation is activated and the substrate is annealed for two hours at 673 K, followed by two hours at 1023 K. After annealing, the chamber is brought to the desired temperature for sample growth. For this analysis films were grown at 295. Flow meters are used to control the flow of oxygen and argon, and the gate valve position is adjusted to bring the system to growth pressure (6 mT for this work). Absolute total pressure in the system was monitored with a MKS Baratron capacitance manometer. Growth is accomplished through the use of an Advanced Energy MDX 500 DC power supply, which controls the current supplied to the uranium target. The current was set at 0.100 A for this growth, which resulted in typical sputter gun powers of ~30 W and voltages of ~300 V. When the proper pressure has been established, film growth is started by turning on the power supply to ignite the uranium target. An Inficon Maxtec TM-400 QCM thickness monitor is utilized to grow films to the desired thickness. After the desired thickness is reached, the power supply is shut off and the film is unloaded from the chamber. The

thickness monitor output is calibrated approximately using thickness values determined using XRR (see Chapter 3). The thickness readings are approximately a factor of 6 larger than the actual film thickness. A full list of equipment used in this analysis can be seen in Table 2.1 below.

Table 2.1: List of equipment used in the magnetron sputtering chamber.

Equipment	Manufacturer	Model
Power Supply	Advanced Energy	MDX 500
Mass Spectrometer	Inficon	Transpector XPR 3
Thickness Monitor	Inficon Maxtek	TM-400
Mass-Flo Controller	MKS	Type 1179A
Mass-Flo Meter	MKS	Type 179A
Capacitance Manometer	MKS	Type 627B
Readout Power Supply	MKS	Type PDR-C-2C
Four-Channel Readout	MKS	Type 247D
Ionization Gauge Tubes	Granville-Phillips	274 Bayard-Alpert type
Vacuum Gauge Contoller	Granville-Phillips	Series 307
Adaptive Pressure Controller	VAT	PM-5
Sample Stage Temperature Controller	AJA International	SHQ-15A PID Heater Control
Sample Stage Motion Controller	AJA International	SXMC Motor Control
Turbo Pump	Leybold Vacuum	Turbo Drive TD20 classic
Turbo Pump Controller	Leybold Vacuum	Turbotronik NT 10
Variable Leak Valve	Varian Vacuum Technologies	951-5106

Figure 2.3: Inconel plate with as-grown Sample 88a and 88b on YSZ substrates.

2.3 Film Growth

Using this reactive-gas sputtering chamber, UO_2 thin films were grown on yittria-stabilized zirconia (YSZ) substrates (1 cm × 1 cm × 0.5 cm). This material was chosen for its excellent urania film growth characteristics and its stability with respect to inter-diffusion at the film-substrate interface [18]. Depleted uranium metal (99.98% purity supplied by Manufacturing Sciences Corp.) was used as the sputtering target. Research grade Ar (99.9999% purity) was used as the sputtering gas. Oxygen was used as the reactive gas, which was supplied from an Ar + O_2 gas bottle (100 ppm O_2). The introduction of ^{18}O to the reactive sputter gas was accomplished with a research grade (99 atom% ^{18}O) gas bottle using a variable leak valve. Oxygen-18 was introduced as a buried tracer layer at the film midplane.

An Inficon Transpector XPR3 mass spectrometer is used to measure the quantities of individual gases during growth. An example of the data output from the mass spectrometer is shown in Figure 2.4. This shows the data produced from the mass spectrometer, which displays the partial pressure of various chosen masses during the growth of Sample 86. For this growth, masses 18, 28, 32, and 40 are displayed. Mass 18 represents the background partial pressure of H_2O in our chamber, but more importantly it represents the partial pressure of ^{18}O when this isotope is introduced. Mass 36 would better quantify ^{18}O; however, ^{36}Ar is a stable isotope of argon with an abundance of 0.34%. This makes a peak difficult to discern when 18O is introduced. Mass 28 represents the partial pressure of nitrogen, mass 32 the partial pressure of oxygen, and mass 40 the partial pressure of argon. At approximately 4 minutes, the uranium gun is ignited, which is evident from the spike in Mass 28. At ignition, uranium nitrides are sputtered from the target surface, which leads to an increased nitrogen partial pressure. Oxygen-18 is introduced at the film midplane until a spike is seen by the mass spectrometer (seen at

approximately 17 minutes in Figure 2.4). Flow is then immediately shut off, in order to produce a narrow peak of ^{18}O. There is a constant increase in the partial pressure of mass 18 throughout growth, which is due to the liberation of water vapor during sputtering. Shortly after 30 minutes the uranium gun in turned off and gas flow is shut off, which is evident from the pressure drop in each mass. The mass spectrometer allows for adjustments to flow rates, of either argon or oxygen, during film growth. Figure 2.5 displays the output during growth and is shown to highlight the ^{18}O peak (seen at approximately 13 minutes).

The most difficult challenge encountered during this project was growing the proper films necessary for this work. Previous work established film growth characteristics for single crystal UO_2 thin films [18]. These films are grown at elevated temperature (973 K) on YSZ. Therefore, to begin we attempted to repeat these growth parameters with a layer of ^{18}O at the film midplane. However, this growth was unsuccessful due to the rather large anion diffusivity of ^{18}O seen at these elevated temperatures. These films did not yield the necessary SIMS profile needed for this work. Multiple other attempts to establish adequate film growth were unsuccessful. These failed attempts include: growing on a sapphire substrate instead of YSZ, growing at slightly less elevated temperatures (773-973 K) on YSZ and introducing ^{18}O at the film midplane, and introducing ^{18}O at elevated temperature after film growth to attempt to establish an adequate profile at the surface. The first growth that was determined to be successful for use in this project was growing UO_2 on YSZ at 295 K and introducing ^{18}O at the film midplane. Sample 80 was first grown without introducing ^{18}O to establish growth parameters on YSZ at 295 K. These same growth parameters were used for sample 82, with ^{18}O introduced at the film midplane. As seen in the Chapter 3, this growth was shown to yield the desired ^{18}O SIMS profile. However, a disadvantage of these growth conditions is that it yields a film that is textured rather than being

single crystal. All additional films used for this analysis were grown at 295 K on YSZ and introducing ^{18}O at the film midplane. However, sample 86 was grown directly after the vacuum chamber had been cleaned and was determined, by XRD, to be single crystal. The oxygen-16 flow rate was adjusted during the growth of this film. The partial pressure of oxygen before ignition was 1×10^{-7} T, at flow rates of 10.0 sccm Ar and 0.8 sccm Ar + O_2. After the uranium gun was ignited, the partial pressure of oxygen dropped, as expected. The flow rate was continually adjusted for the five minutes of growth to establish the desired oxygen-16 partial pressure. The flow rate of Ar + O_2 was raised to 8.0 sccm, while the flow rate of Ar was lowered to 5.0 sccm. This flow rate was maintained for the duration of growth. For sample 88, two films were grown side by side, which produced samples 88a and 88b. Both sample 88a and 88b were determined to once again be a textured film. Sample 91 was grown with the same conditions as sample 88 and was determined to be a textured film. Sample 91 was grown to reproduce results found for sample 91. Film characterization will be discussed in much further detail in Chapter 3.

Table 2.2: Thin film growth conditions and characteristics

Sample		80	82	86		88a	88b	91
Phase		UO_2	UO_2	UO_2		UO_2	UO_2	UO_2
T (K)		295	295	295		295	295	295
Power (W)		33	33	36		35	35	36
Current (A)		0.101	0.101	0.100		0.100	0.100	0.101
Voltage (V)		311	310	345		338	338	344
Flow Rate (sccm)	Ar	10.0	10.0	Initial	10.0	5.0	5.0	0.0
				Final	5.0			
	$Ar+O_2$	2.0	2.0	Initial	0.8	8.0	8.0	10.0
				Final	8.0			
Growth Pressure (mT)	CM1	4.5	4.5	Initial	4.3	6.4	6.4	5.7
				Final	6.2			
	CM2	4.0	4.0	Initial	4.0	5.9	5.9	5.3
				Final	5.8			
$\Delta\Omega$ (degree)	Narrow	N/A	N/A	0.19		N/A	N/A	N/A
	Broad	2.21	2.63	4.39		2.03	2.03	2.25
Thickness (Å)		550	600	600		750	750	750
Crystal Orientation		Textured	Textured	Single-Crystal		Textured	Textured	Textured
$\varepsilon_{[001]}$ [$\times 10^{-3}$]		19	22	14		25	25	24
σ_{unirr}		N/A	18.9 ± 0.2	11.6 ± 0.2		12.9 ± 0.2	11.7 ± 0.4	13.3 ± 0.4

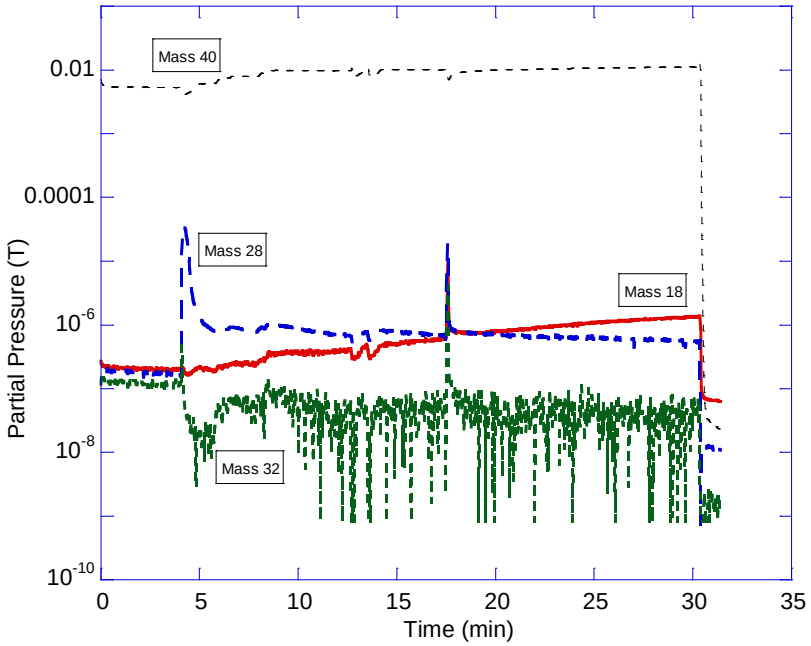

Figure 2.4: Mass spectrometer output during growth of Sample 86. Mass 18 represents ^{18}O, combined with background H_2O in the chamber. Mass 28 represents nitrogen, mass 32 represents oxygen, and mass 40 represents argon. At approximately 4 minutes, the uranium gun is ignited, which is evident from the spike in Mass 28. The second spike in the data, at approximately 17 minutes, represents the introduction of ^{18}O into the chamber in order to place a peak at the film midplane. Shortly after 30 minutes the uranium gun is turned off and gas flow is stopped, which is evident from the pressure drop in each mass.

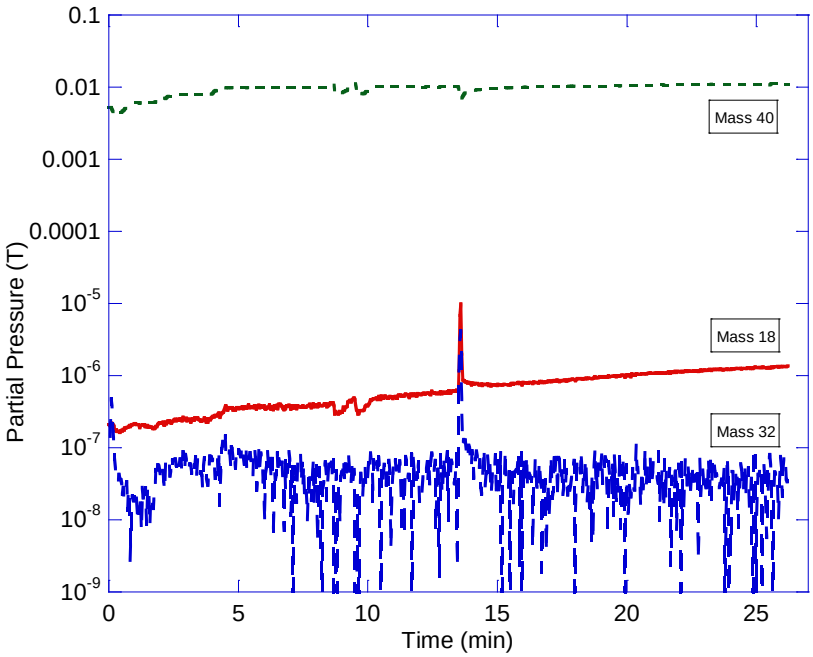

Figure 2.5: Zoomed in mass spectrometer output during growth of Sample 86. Mass 18 represents ^{18}O, combined with background H_2O in the chamber. Mass 32 represents oxygen, while mass 40 represents argon. The spike in the data, at approximately 13 minutes, represents the introduction of ^{18}O into the chamber in order to place a peak at the film midplane.

2.4 Sample Characterization: XRD, XPS, and SIMS

Facilities at the Center for Microanalysis of Materials at the Materials Research Laboratory were used for all sample characterization and irradiation. The center is staffed with experts in each technique and train users to perform their own measurements.

X-ray diffraction (XRD) analysis was performed using a Phillps X'Pert I diffractometer with a Cu K-α1 source ($\lambda = 0.154056$ nm), which is monochromated to reject Cu K-α2. This instrument has very high resolution characteristics (10^{-5} deg.). Diffraction measurements were done for samples both as-grown and post-irradiation. Wide-angle specular 2θ-ω scans, x-ray reflectivity (XRR) scans to measure the film thickness, and Ω rocking curve scans were performed to characterize film characteristics.

X-ray photoelectron spectroscopy (XPS) was performed using a Physical Electronics PHI 5400. This instrument has both Al and Mg x-ray sources for analysis; the aluminum source was chosen for this work. This XPS system uses argon as the sputter gas and has the ability to both sputter and analyze *in situ*. Scans were performed at the surface of each sample, followed by scans at depths at regular intervals. At each depth, first survey scans over the binding energy range of 1100 eV to 0 eV were performed. Survey scans were followed by multiplex scans of the uranium (U-4$f_{7/2}$ and U-4$f_{5/2}$) and oxygen (O-1*s*) regions. Known value of carbon (C-1*s*) was used for binding energy calibration at the surface, while argon (Ar-2*p*) was used for calibration during sputtering.

Secondary-Ion Mass Spectroscopy (SIMS) was performed using a Physical Electronics PHI Trift III. This instrument has excellent mass-resolution and can run in a time-of-flight (TOF) mode, which was done for these measurements. Time-of-flight is a dynamic mode in which the surface is sputtered to determine the concentration of various species as function of depth. This

instrument can detect mass ranges from 0 to 10^4 amu. This instrument can detect impurities at atom densities less than one part per million atomic (ppma) for almost all elements, and 10 ppba for some elements [19]. A 2 keV Cs^- beam was used as the sputtering beam, rastered over an 800 x 800 μm crater. This beam was employed as the sputtering beam to better observe the oxygen depth profiles because cesium bombardment increases the yield of negative ions. A 22 keV Au beam analytical beam was employed with a 100 x 100 μm raster. Depth profiles were measured for both unirradiated and irradiated samples. The same experimental parameters were used in each measurement to ensure consistency of results. An example of a depth profile used for this work is seen in Figure 2.6. Figure 2.7 displays the same depth profile but is normalized by dividing by the total ion intensity at each depth. This takes into account potential matrix effects in the film and inconsistencies in the SIMS measurement, such as current variation. Depth scales were converted from sputtering time to thickness from the previously mentioned XRR measurements (see Chapter 3).

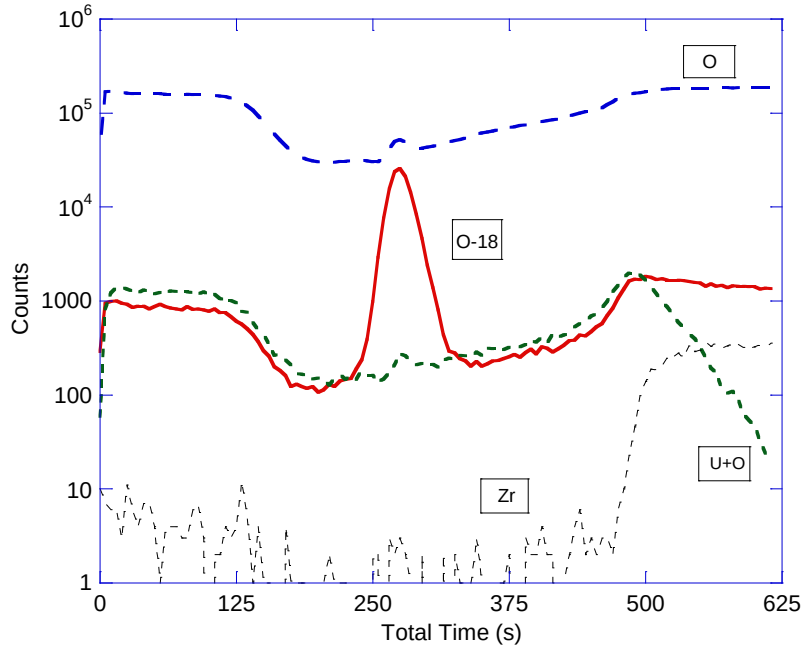

Figure 2.6: A depth profile of as-grown Sample 86, obtained from SIMS. SIMS measurements are given in sputtering time, which varies with each measurement. Therefore, converting from time to thickness is necessary, as described in Chapter 3.

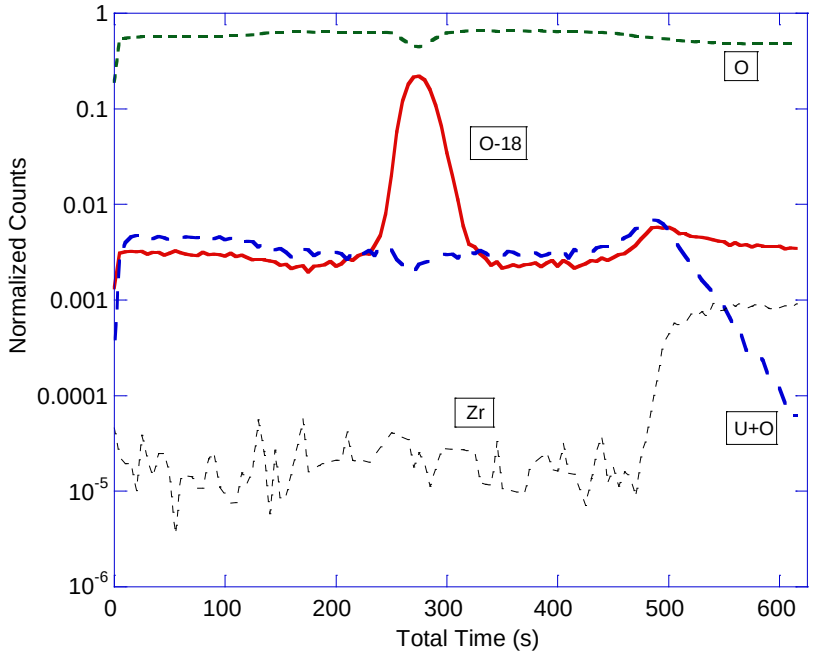

Figure 2.7: A depth profile of as-grown Sample 86, obtained from SIMS. Data from Figure 2.6 has been normalized by total ions. As before, converting from time to thickness is necessary (method is described in Chapter 3).

2.5 Ion Irradiation

Energetic heavy-ion bombardment was performed using the High Voltage Engineering Van de Graaff accelerator at the University of Illinois, shown in Figure 2.8. 1.8 MeV Kr^+ ions were used for irradiation. Each sample was sectioned for simultaneous thermal and irradiation experiments. Two sets of experiments were performed: a set of different doses (fluences) Φ from 0 to 1.0×10^{16} ions/cm^2 at 295 K, and a set at constant dose $\Phi = 1.0 \times 10^{16}$ ions/cm^2 at different temperatures from 295 K to 573 K.

Sample 82 was used for the 295 K irradiations, dose dependence experiments. Sample 82 had a textured microstructure (see Chapter 3). This sample was divided into four 5.0 mm × 5.0 mm sections. The sample was first mounted onto a glass slide using silver paint for good thermal and electrical contact. The glass slide was mounted to a sample stage suited for room temperature measurements (see Figure 2.9). A beam current of 100 nA over a 4.5 mm × 4.5 mm beam aperture was used for irradiation. The 4.5 mm × 4.5 mm beam aperture was used to irradiate each 5.0 mm × 5.0 mm section of the film. The beam was aligned to two edges of the film to ensure bombardment occurred on one section of the film. To ensure beam stability, a Faraday cup was inserted into the beam path, and the current was verified at 5 minute intervals during irradiation. For 295 K experiments, irradiation time ranged from 32 seconds to 54 minutes. For the first experiment four doses were chosen: 1.0×10^{14}, 1.0×10^{15}, 5.0×10^{15}, and 1.0×10^{16} ions/cm^2. The 1.0×10^{14} ions/cm^2 dose yielded poor results and this data is not presented here. After SIMS analysis, these same sections were exposed to further irradiation. For example the section which received a dose of 1.0×10^{15} ions/cm^2 was exposed to an additional 2.0×10^{15} ions/cm^2, for a total of 3.0×10^{15} ions/cm^2. A dose of 2.0×10^{16} ions/cm^2 was performed, but the ^{18}O peak was

altered by interaction with the substrate. Due to this interaction, the shape of the ^{18}O peak could not be fit accurately with a Gaussian distribution; this analysis is also omitted here.

For the constant dose experiments, temperature dependence measurements, the same beam current and aperture size as above were used. The temperature range allowed for these experiments was fairly limited due to the high anion diffusivity at elevated temperatures. For this reason, experiments were conducted up to 573 K. A dose of 1.0×10^{16} ions/cm^2 was used for these experiments, which required an irradiation time of 54 minutes at a current of 100 nA. Samples 86, 88, and 91 were used for these measurements. After growth, each sample was sectioned into three 10 mm × 3.3 mm sections. A single 10 mm × 3.3 mm section was attached directly to a low-temperature stage using silver paint, as shown in Figure 2.10. The sample stage used here can be heated to 873 K. A thermocouple is attached to a screw on the stage, located directly to the sample. The same 4.5 × 4.5 mm aperture was used, which allowed for half of each sectioned sample to be irradiated, while the other half was unirradiated for the thermal-only diffusivity. The beam was positioned to be centered on one 5 mm × 3.3 mm section of each sample, which left the other 5 mm × 3.3 mm section unexposed to the beam. This method allowed both halves of the sample to be exposed to the same thermal history. Sample 86 was irradiated at a dose of 1.0×10^{16} ions/cm^2 at: 295 K, 393 K, 473 K, 573 K, and 623 K. The corresponding thermal measurements at these three temperatures were also taken. Samples 88a and 88b were irradiated at a dose of 1.0×10^{16} ions/cm^2. Sample 88a was irradiated at 295 K, 393 K, and 473 K; sample 88b was irradiated at 573 K and 623 K. Sample 91 was irradiated at a dose of 1.0×10^{16} ions/cm^2 at: 295 K, 393 K, 473 K, and 573 K. Samples were irradiated at the same temperatures to compare the radiation enhanced diffusivity and thermal diffusivity.

Figure 2.8: High Voltage Van de Graaff Accelerator at the University of Illinois.

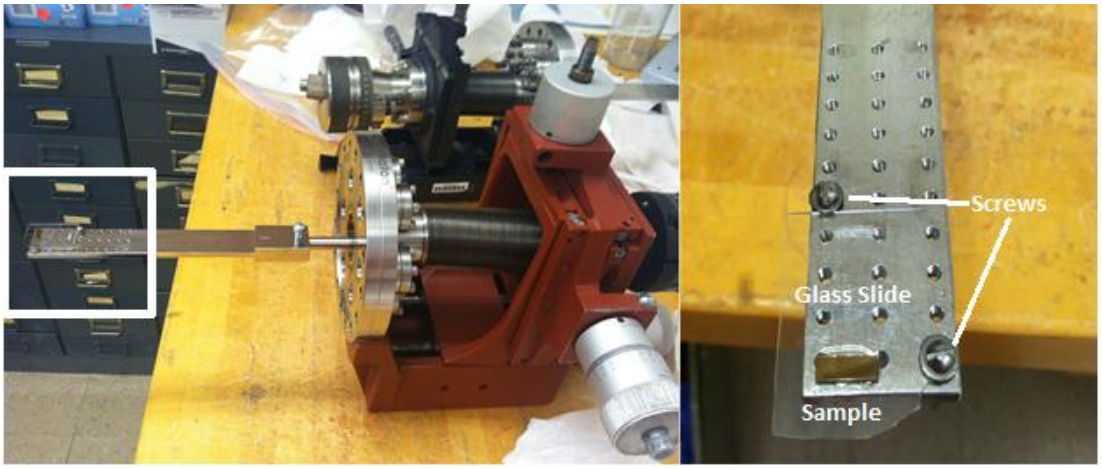

Figure 2.9: Photograph of the sample stage used for room temperature irradiations. Left: A photograph of the entire stage. Right: Magnified view showing a sample mounted to a glass slide, which is then mounted to the sample stage with screws.

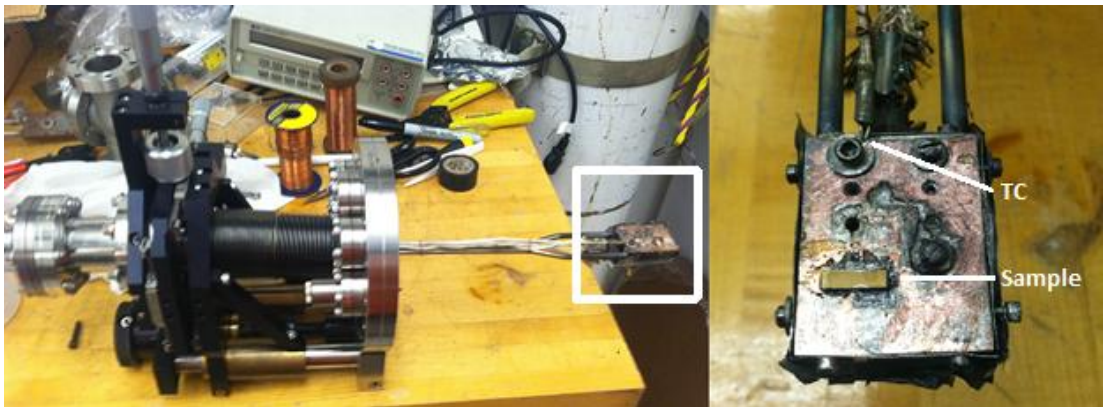

Figure 2.10: Photograph of the sample stage used for elevated temperature irradiations. This stage is suitable for use up to 873 K. Left: A photograph of the entire stage. Right: Magnified view showing a sample mounted directly to the sample stage, with thermocouple (TC) location shown.

Table 2.3: Irradiation characteristics for Sample 82

T [K]	t [sec]	Dose [ions/cm^2]
295	0	0
295	324	1.00E+15
295	972	3.00E+15
295	1620	5.00E+15
295	3240	1.00E+16

Table 2.4: Irradiation characteristics for Sample 86

T [K]	t [sec]	Dose [ions/cm^2]
295	0	0
295	3240	1.00E+16
393	0	0
393	3240	1.00E+16
473	0	0
473	3240	1.00E+16
573	0	0
573	3240	1.00E+16
623	3240	1.00E+16

Table 2.5: Irradiation characteristics for Sample 88

T [K]	t [sec]	Dose [ions/cm^2]
295^{+}	0	0
295^{+}	3240	1.00E+16
393^{+}	0	0
393^{+}	3240	1.00E+16
473^{+}	0	0
473^{+}	3240	1.00E+16
573^{++}	0	0
573^{++}	3240	1.00E+16
623^{++}	0	0
623^{++}	3240	1.00E+16

$^{+}$ Sample 88a
$^{++}$ Sample 88b

Table 2.6: Irradiation characteristics for Sample 91

T [K]	t [sec]	Dose [ions/cm^2]
295^{+}	0	0
295^{+}	3240	1.00E+16
393^{+}	3240	1.00E+16
473^{+}	0	0
473^{+}	3240	1.00E+16
573^{++}	0	0
573^{++}	3240	1.00E+16

CHAPTER 3: RESULTS

3.1 XRD and XRR Results

To be considered single crystal a thin film must satisfy the following conditions: preferred or highly textured out-of-plane growth, as characterized by specular scans; in-plane φ or rotational scans signifying a single growth domain; and narrow rocking curve or mosaic width signifying a commensurate crystal lattice without large-angle tilt boundaries [19]. Strehle *et al.* characterized single crystal growth of UO_2 thin films on YSZ [19]. Films used in their analysis were grown at 650-700 ºC. Specular 2θ-ω scans displayed (0 0 2), (0 0 4), and (0 0 6) peaks, indicating a preferential growth direction in the [0 0 1] direction. In-plane φ scans demonstrated four-fold symmetry. Rocking curves displayed $\Delta\Omega \sim 0.1^{\circ}$ for the narrow component and $\Delta\Omega \sim 1^{\circ}$ for the broad component [19].

As stated previously, UO_2 thin films grown for use in this analysis were grown on YSZ at RT and introducing ^{18}O at the film midplane. As seen in Figure 3.1, films used in this analysis display the same (0 0 2) and (0 0 4) peaks, indicating a preferential growth direction in the [0 0 1] direction. The (0 0 6) peak is also seen but has been omitted from these plots for convenience of comparison. However, the (1 1 1) UO_2 reflection is seen. This peak is of much lower intensity than the peaks in the [0 0 1] direction. This specular scan is indicative of a textured film, since diffraction intensity is displayed for reflections other than the higher order primary reflections. The two strong, narrow peaks are from the YSZ substrate. Each film used in this analysis (80, 82, 86, 88, and 91) displayed the same four film peaks.

Figure 3.2 displays a comparison of rocking curves around the (0 0 2) plane position. Sample 80, 82, 88, and 91 displayed only a broad component of $\Delta\Omega \sim 2^{\circ}$. However, sample 86 displayed both a narrow $\Delta\Omega \sim 0.2^{\circ}$ and a broad component $\Delta\Omega \sim 4^{\circ}$. The rocking curve for sample 86 is

similar to the previous work [19], and it satisfies one condition necessary for the thin film to be considered single crystal. Figure 3.3 displays a comparison of in-plane φ scans. Samples 80, 82, 88, and 91 displayed featureless in-plane phi scans, which are expected of textured films. However, sample 86 displayed four distinct peaks, each separated 90° apart. This demonstrates four-fold symmetry expected for (*l l l*) reflections of UO_2. The in-plane φ scan, which signified a single growth domain, couple with a narrow rocking curve or mosaic width, which signified a commensurate crystal lattice without large-angle tilt boundaries, led to the conclusion that Sample 86 was single crystal. This result was unexpected, since single crystal growth is thought to require high growth temperatures. Sample 86 was grown directly after the magnetron sputtering chamber had been cleaned. This cleaning process could have contributed to this single crystal growth. The chamber would have been rid of various impurities that are generally found in the sputtering chamber, which could have promoted single crystal growth.

Figure 3.4 displays a typical XRR measurement observed in this analysis. This reflectivity measurement is of sample 80. From this measurement, a fitting program is used to determine the film thickness; in this case the thickness was determined to be 600 Å. The film thickness is important to this analysis, especially in setting the depth scale for SIMS measurements (which will be discussed later in this chapter).

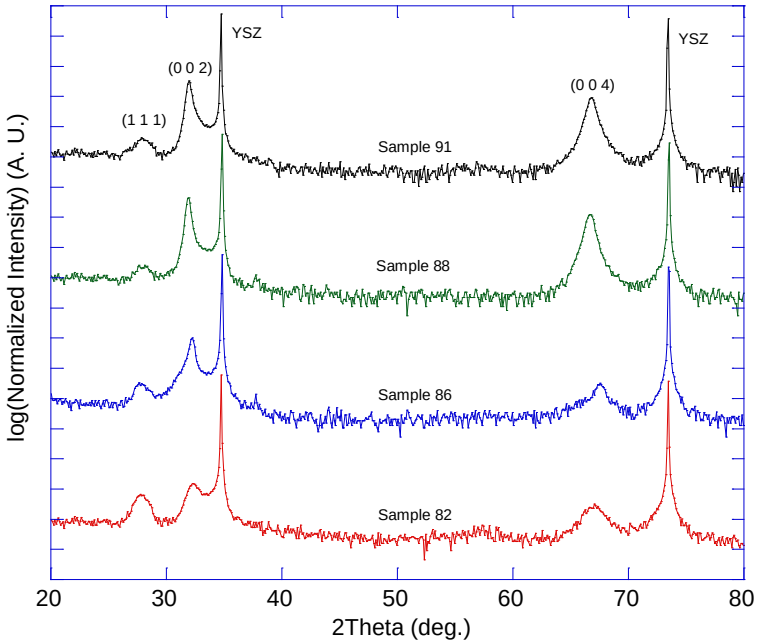

Figure 3.1: Normalized specular 2θ-ω scans, obtained from XRD measurements, showing the (1 1 1), (0 0 2), and (0 0 4) reflections. The (0 0 6) peaks are not shown here for the convenience of comparison. Each specular scan has been normalized to the area under the entire spectrum. An intensity scale graduated in power of ten has been plotted and each curve has been shifted vertically for clarity.

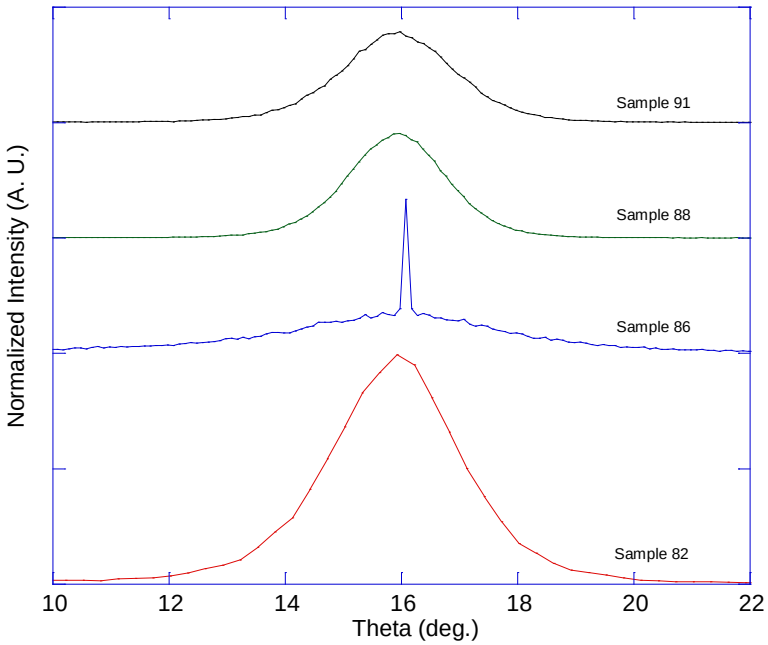

Figure 3.2: A comparison of the rocking curves, obtained from XRD, of the samples used in this analysis. A narrow component is only seen in sample 86. Each rocking curve has been normalized to the area under its respective curve. A linear intensity scale has been plotted and each curve has been shifted vertically for clarity.

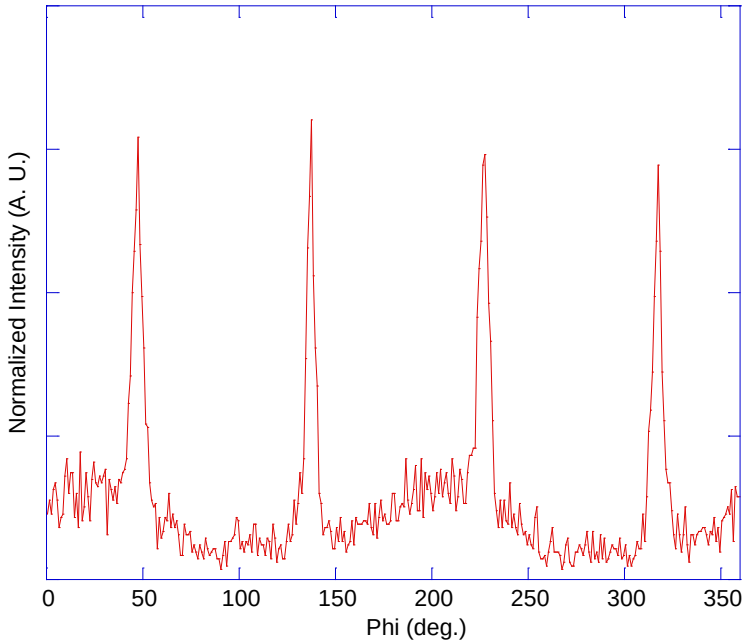

Figure 3.3: In-plane φ scan for sample 86. Four distinct peaks are displayed, each separated by 90°. This result demonstrates four-fold symmetry expected for (*l l l*) reflections of UO_2. This measurement has been normalized to the area under the curve, and a linear intensity scale has been plotted.

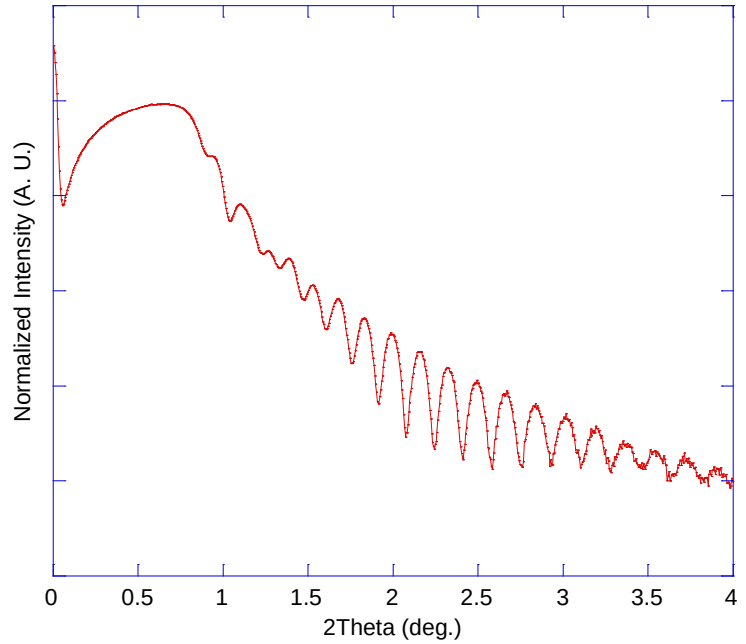

Figure 3.4: A typical XRR measurement of the samples used in this analysis. This measurement is used to calculate the film thickness. This parameter allows the SIMS depth scale to be set. This measurement has been normalized to the area under the curve and has been plotted with the intensity scale graduated in powers of ten.

3.2 XPS Results

Figure 3.5a and 3.5b display an XPS analysis of the U-4*f* binding energy ranges as a function of sputter depth for sample 80. The first scan shown is a scan of the film surface. UO_2 has been shown to readily oxidize in air to higher oxygen stoichiometry [20]. Therefore, *in situ* sputtering is necessary to remove this higher surface oxide layer and properly quantify the uranium valency. The Physical Electronics PHI 5400, used in this analysis, is capable of both sputter and analysis *in situ*. However, sputtering introduces an unavoidable consequence known as preferential sputtering [20]. Lighter species are preferentially sputtered, which means that oxygen atoms will be sputtered at a faster rate than the heavier uranium atoms. As seen in Figure 3.5a, the removal of surface oxidation corresponds to a shift to lower binding energies in the U-4*f* valence state. This was shown to be consistent with a higher oxidation state (U_3O_7 or U_3O_8) at the surface [20]. In addition, 4+ shake-up satellite peaks are observed after surface oxide removal, which are absent in U_3O_8 spectra [20]. The dotted lines in Figure 3.5a and 3.5b display peak positions at the depth of 10 Å. Data was fit with CasaXPS processing software. Peak positions are shown to shift to higher binding energies as a function of depth. Sputter erosion results in an increase of the U-4f electron binding energy by ~1 eV, which is displayed in Table 3.1. This shift was shown to be consistent with a change in charge carrier from acceptor sites (p-type semiconductor behavior) to donor sites (n-type semiconductor behavior) [19]. The solid vertical line marks the formation of a metallic U-4$f_{5/2}$ peak. This formation is attributed to the preferential sputtering of oxygen, which leads to a reduction of oxygen stoichiometry and formation of a metallic component in the U-4*f* region. This metallic peak is shown to become stronger with as a function of depth, which can be seen in Figure 3.5b. At 300 Å depth, the intensity of the metallic uranium component is greater than the U-4$f_{7/2}$ peak.

Figure 3.6a and 3.6b displays the O-1*s* valence state as a function of sputter depth for sample 80. The surface scan contains peak at ~530 eV. This scan also contains a broader leading edge, which is eliminated with sputtering. The dotted line marks the reference location of the O-1*s* peak at a depth of 10 Å. Peaks are shifted to higher binding energies as a function of depth, due to preferential sputtering.

Figure 3.7 displays an XPS analysis comparing samples 86 and 88a of the U-4*f* binding energy ranges as a function of sputter depth. Figure 3.8 displays an XPS analysis of the O-1*s* binding energy ranges as a function of sputter depth comparing samples 86 and 88a. Since virgin samples were unavailable, samples 86 and 88a were used for these measurements, which were previously exposed to 473 K and 393 K thermal measurements, respectively. Data was fit with CasaXPS processing software. U^{4+} ($4f_{7/2}$) peak locations are shown in Table 3.2. Peak locations at each sputter depth are nearly identical. There is not a significant difference in the uranium valency between the single crystal and textured samples.

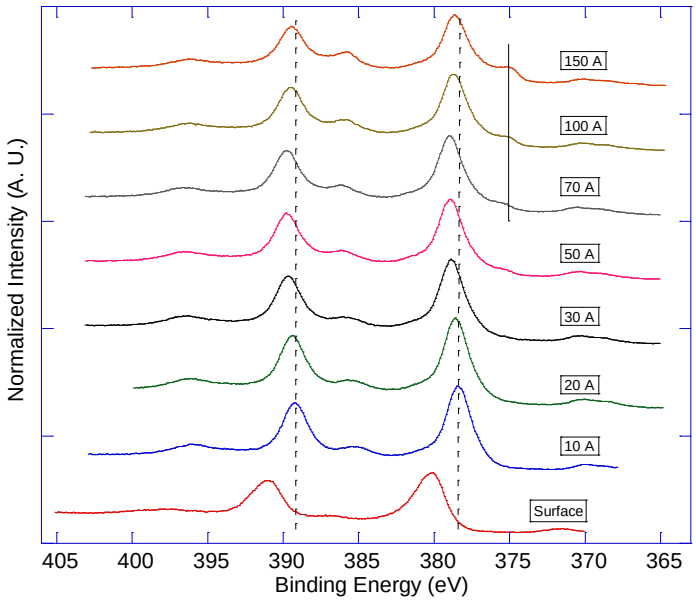

Figure 3.5a: XPS analysis of the U-4*f* binding energy ranges as a function of sputter depth for sample 80. Surface scan has been calibrated using the known C-1*s* peak at 285.1 eV. At each depth, scans have been calibrated using the known Ar-2*p* peak at 241.8 eV. The dotted lines mark the reference location of the 10 Å depth peak for relative binding energy shifts of the other measurements. The solid vertical line marks the formation of metallic U peak that evolves due to preferential sputtering. A linear intensity scale has been plotted and each curve has been shifted vertically for clarity.

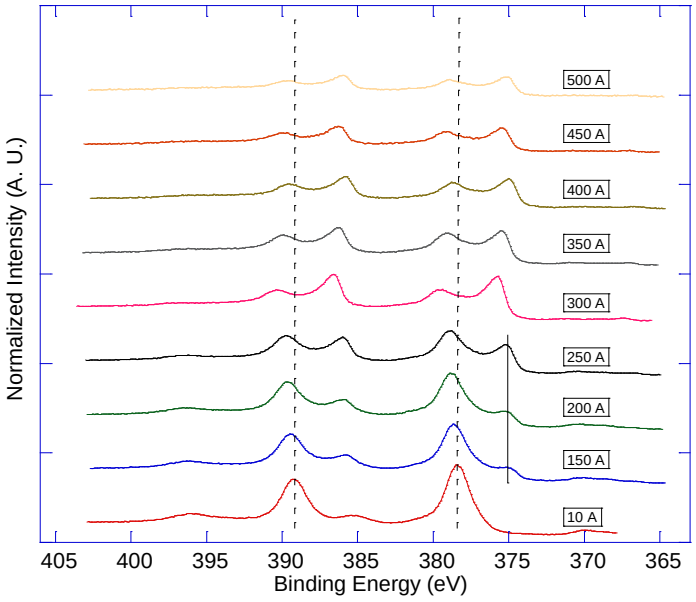

Figure 3.5b: XPS analysis of the U-4*f* binding energy ranges as a function of sputter depth for sample 80. Surface scan has been calibrated using the known C-1*s* peak at 285.1 eV. At each depth, scans have been calibrated using the known Ar-2*p* peak at 241.8 eV. The dotted lines mark the reference location of the 10 Å depth peak for relative binding energy shifts of the other measurements. The solid vertical line marks the formation of metallic U peak that evolves due to preferential sputtering. A linear intensity scale has been plotted and each curve has been shifted vertically for clarity.

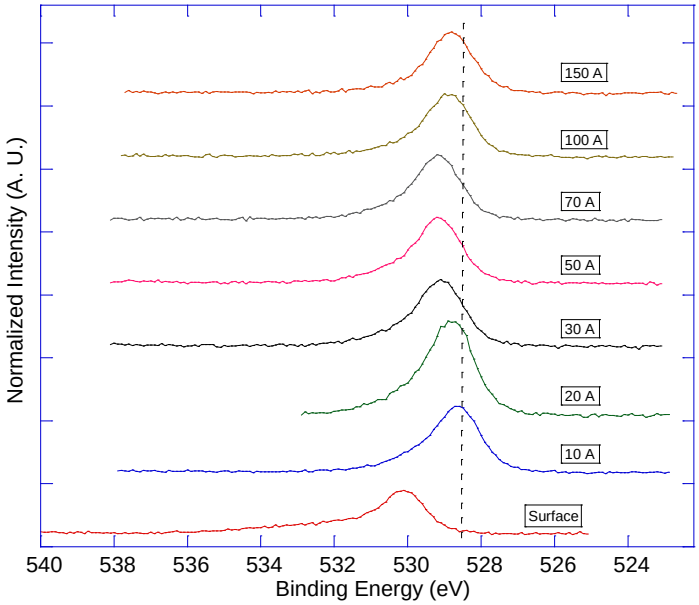

Figure 3.6a: XPS analysis of the O-1*s* binding energy ranges as a function of sputter depth for sample 80. Surface scan has been calibrated using the known C-1*s* peak at 285.1 eV. At each depth, scans have been calibrated using the known Ar-2*p* peak at 241.8 eV. The dotted line marks the reference location of the 10 Å depth peak for relative binding energy shifts of the other measurements. A linear intensity scale has been plotted and each curve has been shifted vertically for clarity.

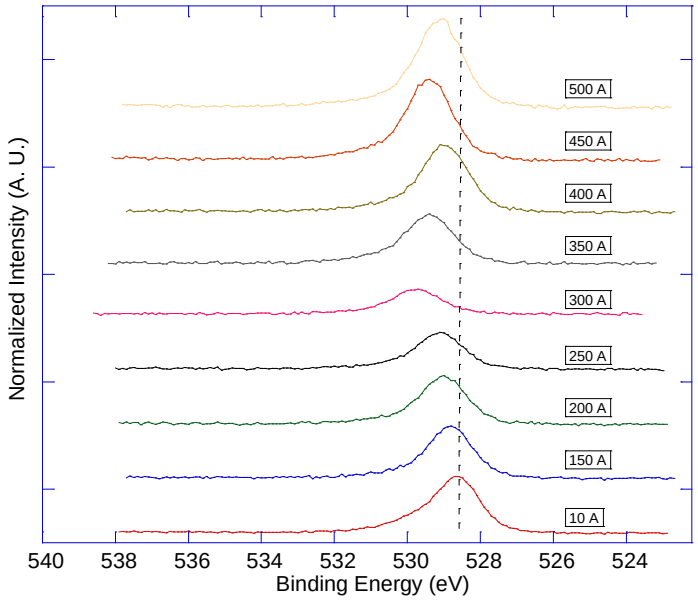

Figure 3.6b: XPS analysis of the O-1*s* binding energy ranges as a function of sputter depth for sample 80. Surface scan has been calibrated using the known C-1*s* peak at 285.1 eV. At each depth, scans have been calibrated using the known Ar-2*p* peak at 241.8 eV. The dotted line marks the reference location of the 10 Å depth peak for relative binding energy shifts of the other measurements. A linear intensity scale has been plotted and each curve has been shifted vertically for clarity.

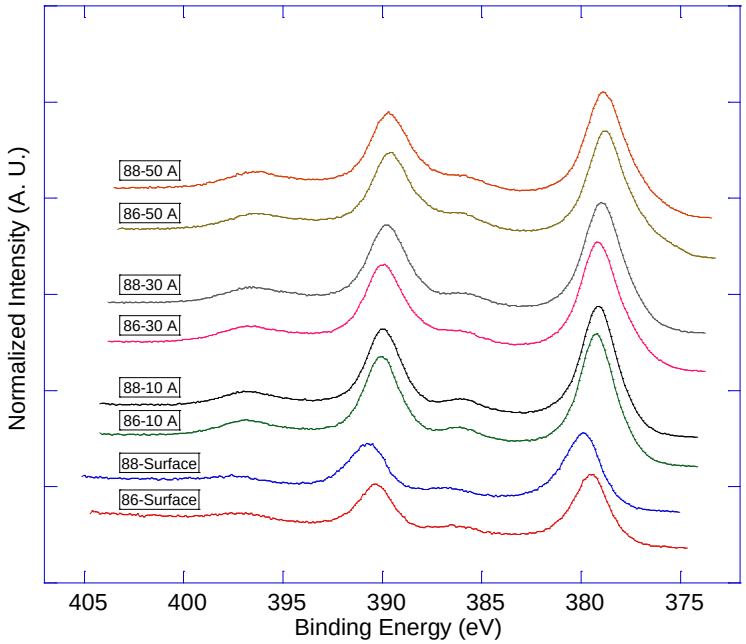

Figure 3.7: XPS analysis of the U-4*f* binding energy ranges as a function of sputter depth comparing samples 86 and 88a. Sample 86 was previously exposed to a 473 K thermal measurement, while sample 88a was previously exposed to a 393 K thermal measurement. Surface scan has been calibrated using the known C-1*s* peak at 285.1 eV. At each depth, scans have been calibrated using the known Ar-2*p* peak at 241.8 eV.

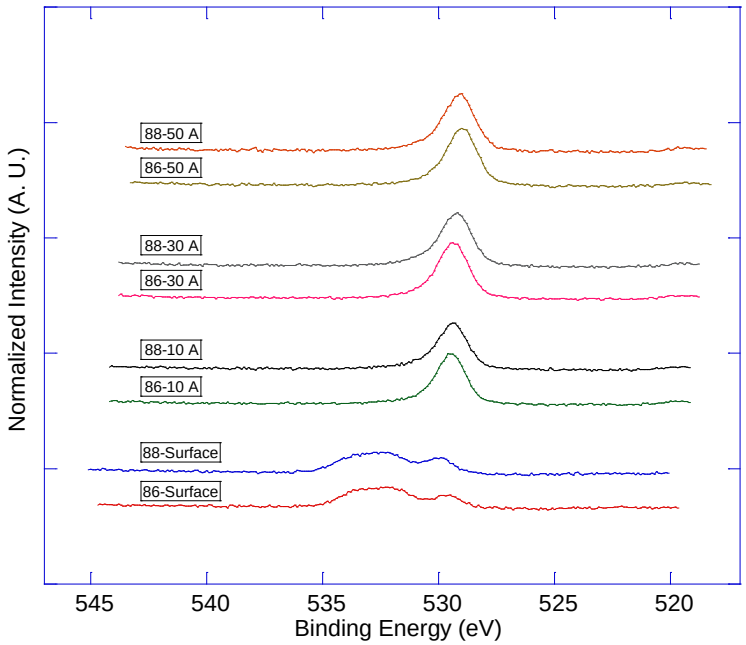

Figure 3.8: XPS analysis of the O-1*s* binding energy ranges as a function of sputter depth comparing samples 86 and 88a. Sample 86 was previously exposed to a 473 K thermal measurement, while sample 88a was previously exposed to a 393 K thermal measurement. Surface scan has been calibrated using the known C-1*s* peak at 285.1 eV. At each depth, scans have been calibrated using the known Ar-2*p* peak at 241.8 eV.

Table 3.1: XPS data for Samples 80, as a function of depth.

Depth	U^{4+} ($4f_{7/2}$) Component (±0.3 eV)	FWHM	U^{6+} ($4f_{7/2}$) Component (±0.3 eV)	FWHM	Metallic Location
10	378.3	2.1	None	N/A	None
20	378.5	2.2	None	N/A	None
30	378.8	2.2	None	N/A	None
50	378.9	2.0	None	N/A	None
70	378.9	2.0	381.3	1.42	374.5
100	378.7	2.0	381.0	1.43	374.8
150	378.6	1.9	380.9	1.49	374.6
200	378.8	1.9	381.1	1.47	374.9
250	379.0	1.7	381.0	1.79	375.0
300	379.7	1.5	381.5	2.12	375.7
350	379.2	1.5	380.8	2.40	375.4
400	378.8	1.4	380.0	2.67	374.9
450	379.3	1.6	381.2	2.00	375.4
500	379.1	1.3	380.3	2.15	375.1

Table 3.2: Comparison of XPS data for Samples 86 and 88a, as a function of depth.

Sample	Depth [Å]	U-$4f_{7/2}$ Peak Energy (±0.3 eV)	FWHM (eV)	Metallic Location (eV)
86	10	379.1	2.2	None
88a	10	379.0	2.2	None
86	30	379.0	2.5	None
88a	30	378.8	2.4	None
86	50	378.8	2.1	376.8
88a	50	378.9	2.1	377.2

3.3 SIMS/Ion Irradiation Results

Table 3.3 displays data for unirradiated/as-grown samples used in this analysis. Oxygen-18 was introduced at the film midplane in samples 82, 86, 88a, 88b, and 91. Films 88a and 88b were grown simultaneously, with two substrates placed next to each other on the Inconel plate. These samples were grown with identical growth conditions, which allowed for a greater number of experiments. However, these were grown on separate substrates and thus were named 88a and 88b. A functioning mass spectrometer was used in the growth of samples 86, 88a, 88b, and 91. This mass spectrometer allowed greater control of the amount of ^{18}O introduced into these films. As seen in Table 3.3, narrower ^{18}O peaks were produced. A narrow unirradiated tracer peak is desired in RED measurements because it allows for higher dose and higher temperature measurements before the peak becomes too broad to analyze.

For each SIMS depth profile, the total sputtering time varies slightly for each measurement. To account for this, the depth scale is changed from time to thickness. The depth scale is set by the following method: the point at which the Zr peak (the strongest peak associated with the YSZ substrate) is half its maximum value is taken to be the film and substrate interface. The distance from zero depth to this interface is considered the total film thickness. This thickness was obtained from XRR results (stated previously and determined to be 600 Å for sample 82). The x-axis scale was the converted from sputtering time to depth, from the ratio of total thickness to total sputtering time. Heavy-ion bombardment can result in sputtering as much as 10-50 Å of the film. It is therefore assumed that the distance from the center of the peak to the film/substrate interface is unaltered during irradiation. For each irradiated sample, the center of the ^{18}O peak is placed at the same depth as for the unirradiated sample. Therefore, we are able to convert sputtering time to depth for each irradiated sample. An example of this can be seen in Figure 3.9.

Figure 3.10 displays room temperature ^{18}O depth profiles, measured by SIMS, for sample 82. A total of five curves have been plotted: an unirradiated profile and four irradiated profiles. Each depth profile was fit with a Gaussian distribution. Each ^{18}O peak has been normalized by setting the area under the curve to be equal to 1 for each profile. Since the same sample was used for each profile (sample 82 was divided into regions for irradiation), it is assumed that the total ^{18}O content is the same in each sample. The loss of ^{18}O is not expected to occur during heavy ion bombardment. Figure 3.10 displays the changes induced by irradiation. Increased broadening is seen at each subsequent dose. This broadening is measured quantitatively by fitting a Gaussian distribution to each profile. Standard deviations, σ, are calculated from each distribution and have been tabulated in Table 3.4. An increase in standard deviation with dose is expected and confirmed by the room temperature results.

Samples 86, 88a, 88b, and 91 were exposed to ion irradiation at elevated temperatures. Samples were cut into 10 mm × 3.3 mm sections (as discussed in Chapter 2). The beam was positioned to be centered on one 5 mm × 3.3 mm section of each sample, which left the other 5 mm × 3.3 mm section unexposed to the beam. This method allowed both halves of the sample to be exposed to the same thermal history. Figure 3.11 displays the set of thermal diffusion measurements for sample 86 and Figure 3.12 displays the set of thermal diffusion measurements for samples 88a and 88b. The depth scale has been inverted so that zero depth corresponds to the film half-width and the center of the ^{18}O profiles, with the leading edge shown. These profiles have been normalized by setting the area under the curve to be equal to 1 and have been fit to a half-Gaussian. Standard deviations for each profile are shown in Table 3.5, Table 3.6, and Table 3.7 for samples 86, 88 (a and b), and 91, respectively.

Figure 3.13 displays the set of at-temperature irradiations for sample 86 and Figure 3.14 displays the set of at-temperature irradiations for samples 88a and 88b. Each section of the sample was exposed to a constant dose of 1.0×10^{16} ions/cm^2. Leading edges are once again shown, which have been fit to a half-Gaussian. Standard deviations for each profile are shown in Table 3.5, Table 3.6, and Table 3.7 for samples 86, 88 (a and b), and 91, respectively.

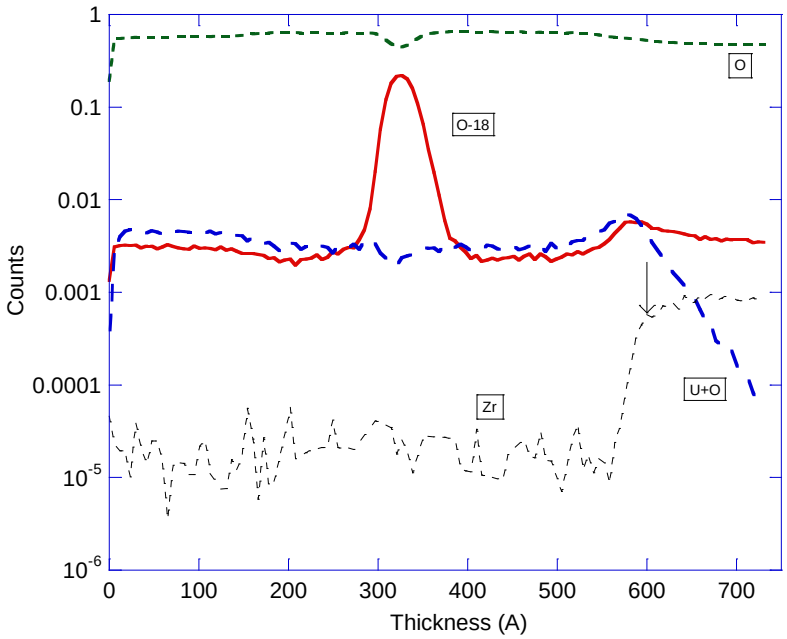

Figure 3.9: A depth profile of as-grown Sample 86, obtained from SIMS. Data has been converted from sputtering time to depth, using the method described above. The arrow indicates the film/substrate interface, which occurs at approximately 600 Å.

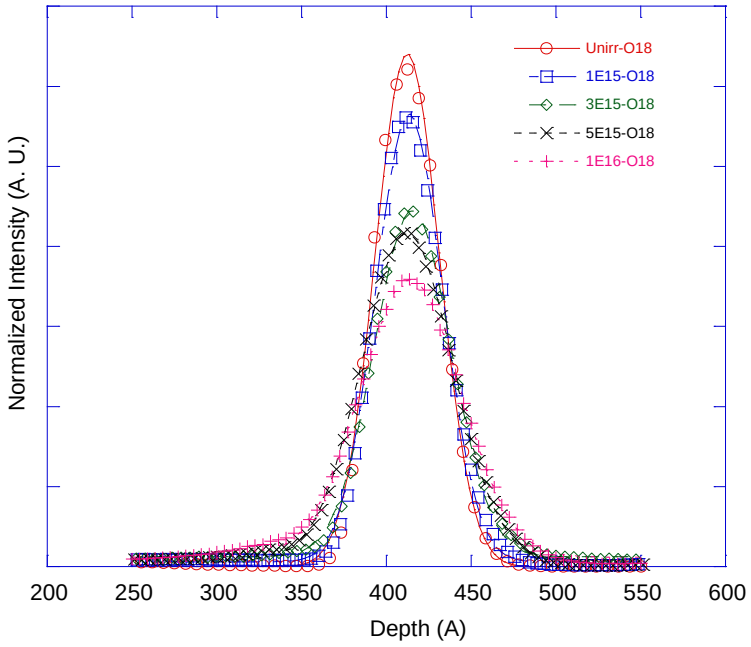

Figure 3.10: Normalized ^{18}O depth profiles for sample 82, irradiated at room temperature to fluences (in units of ions/cm^2) as indicated. Gaussian distributions were fit to each profile, which are indicated by the solid lines. Standard deviations from these fits can be seen in Table 3.4. This measurement has been normalized to the area under the curve, and a linear intensity scale has been plotted.

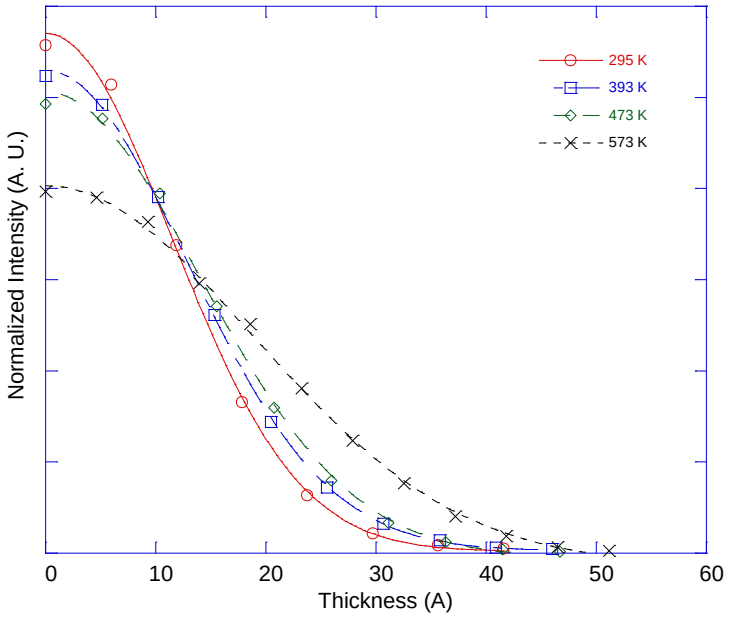

Figure 3.11: Normalized ^{18}O depth profiles for sample 86, unirradiated and used for thermal diffusion measurements. The depth scale is inverted so that zero depth corresponds to the film half-width and the center of the ^{18}O profiles. Half-Gaussian distributions were fit to the leading edge of each profile, which are indicated by the solid lines. Standard deviations from these fits can be seen in Table 3.5. This measurement has been normalized to the area under the curve, and a linear intensity scale has been plotted.

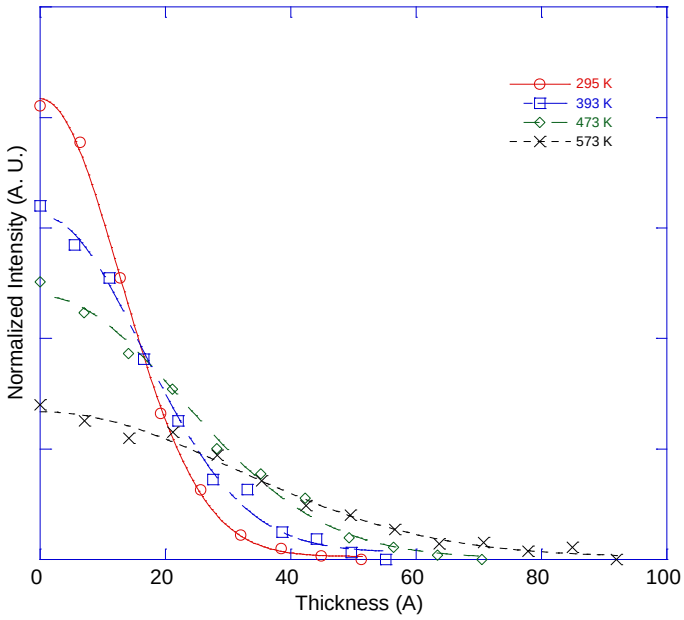

Figure 3.12: Normalized ^{18}O depth profiles for sample 88, unirradiated and used for thermal diffusion measurements. Sample 88a was used for the 295 K, 393 K, and 473 K measurements. Sample 88b was used for the 573 K measurements. The depth scale is inverted so that zero depth corresponds to the film half-width and the center of the ^{18}O profiles. Half-Gaussian distributions were fit to the leading edge of each profile, which are indicated by the solid lines. Standard deviations from these fits can be seen in Table 3.6. This measurement has been normalized to the area under the curve, and a linear intensity scale has been plotted.

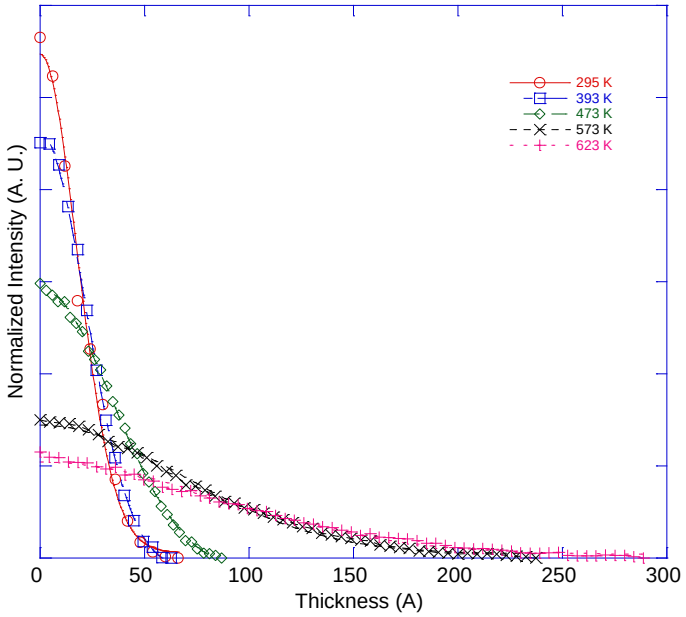

Figure 3.13: Normalized ^{18}O depth profiles for sample 86, irradiated at the temperatures indicated above at a dose of 1.0×10^{16} ions/cm^2. The depth scale is inverted so that zero depth corresponds to the film half-width and the center of the ^{18}O profiles. Half-Gaussian distributions were fit to the leading edge of each profile, which are indicated by the solid lines. Standard deviations from these fits can be seen in Table 3.5. This measurement has been normalized to the area under the curve, and a linear intensity scale has been plotted.

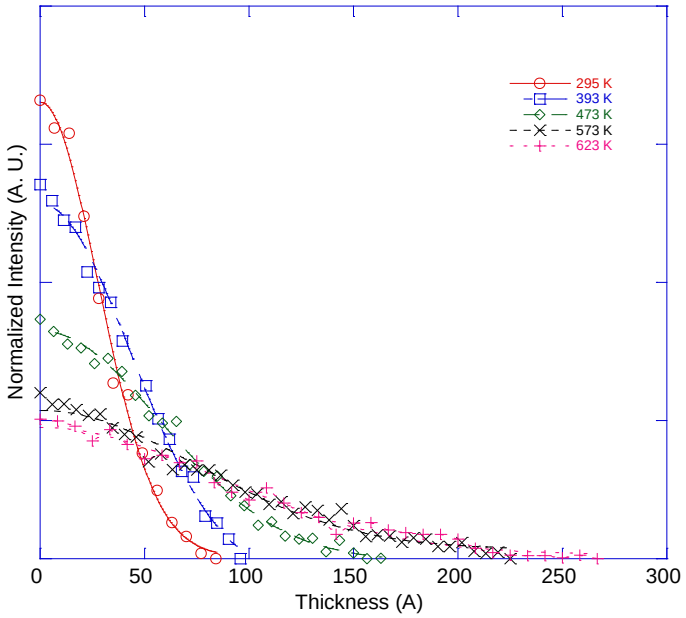

Figure 3.14: Normalized ^{18}O depth profiles for sample 88, irradiated at the temperatures indicated above at a dose of 1.0×10^{16} ions/cm^2. Sample 88a was used for the 295 K, 393 K, and 473 K measurements. Sample 88b was used for the 573 K and 623 K measurements. The depth scale is inverted so that zero depth corresponds to the film half-width and the center of the ^{18}O profiles. Half-Gaussian distributions were fit to the leading edge of each profile, which are indicated by the solid lines. Standard deviations from these fits can be seen in Table 3.6. This measurement has been normalized to the area under the curve, and a linear intensity scale has been plotted.

Table 3.3: Properties of unirradiated/as-grown samples.

Sample	Thickness [Å]	σ_{unirr} [Å]
82	600	18.9 ± 0.2
86	600	11.6 ± 0.2
88a	750	12.9 ± 0.2
88b	750	11.7 ± 0.4
91	750	13.3 ± 0.4

Table 3.4: Irradiation conditions and measured ^{18}O profile standard deviations for sample 82.

T [K]	t [s]	Φ [1/Å^2]	σ [Å]
295	0	0	18.9 ± 0.2
295	324	0.1	19.8 ± 0.2
295	324	0.1	19.6 ± 0.2
295	972	0.3	22.7 ± 0.2
295	1620	0.5	26.7 ± 0.2
295	3240	1.0	29.5 ± 0.2

Table 3.5: Irradiation conditions and measured ^{18}O profile standard deviations for sample 86.

T [K]	t [s]	Φ [1/Å^2]	σ [Å]
295	0	0	11.6 ± 0.2
295	3240	1.0	18.1 ± 0.2
393	0	0	12.9 ± 0.1
393	3240	1.0	21.7 ± 0.3
473	0	0	13.8 ± 0.2
473	3240	1.0	34.6 ± 0.3
573	0	0	18.0 ± 0.2
573	3240	1.0	68.3 ± 0.9
623	3240	1.0	86.1 ± 1.3

Table 3.6: Irradiation conditions and measured ^{18}O profile standard deviations for sample 88a and sample 88b.

T [K]	t [s]	Φ [1/Å^2]	σ [Å]
295*	0	0	12.9 ± 0.2
295**	0	0	11.7 ± 0.4
295*	3240	1.0	27.6 ± 1.1
393*	0	0	16.3 ± 0.6
393*	3240	1.0	43.4 ± 1.8
473*	0	0	22.5 ± 1.0
473*	3240	1.0	57.8 ± 1.6
573**	0	0	31.1 ± 1.6
573**	3240	1.0	75.0 ± 2.9
623**	3240	1.0	85.7 ± 3.4

* Sample 88a
** Sample 88b

Table 3.7: Irradiation conditions and measured ^{18}O profile standard deviations for sample 91.

T [K]	t [s]	Φ [1/Å^2]	σ [Å]
295	0	0	13.3 ± 0.4
295	3240	1.0	25.0 ± 0.4
393	3240	1.0	40.6 ± 1.1
473	0	0	21.5 ± 0.2

CHAPTER 4: ANALYSIS

4.1 Mixing Parameter

As defined in Chapter 1, a measure of diffusion during irradiation is the mixing parameter, which is defined as,

$$\xi = \frac{Dt}{\Phi F_D} \quad (4.1)$$

where D is the diffusion coefficient [cm^2/sec], t is irradiation time [sec], Φ is the ion fluence [ions/cm^2], and F_D [eV/cm/ion] is the nuclear differential energy deposited. The product Dt is known as the total mean square displacement and can be defined as,

$$2Dt = (\sigma_{irr})^2 - \left(\sigma_{ref}\right)^2 \quad (4.2)$$

where σ is defined as the standard deviation obtained from fitting ^{18}O peaks with a Gaussian distribution. To calculate the mixing parameter, standard deviations for both as-grown (σ_{ref}) and irradiated (σ_{irr}) samples were calculated. For mixing parameter calculations at 295 K, σ_{ref} indicates as-grown, unirradiated samples; whereas, σ_{irr} indicates irradiated samples at varying doses. The product ΦF_D is the total differential energy deposition. Using TRIM calculations, $F_D \approx 130$ eV/Å/ion for a UO_2 thin film exposed to 1.8 MeV Kr^+, which is seen in Figure 4.1.

Sample 82 was irradiated at 295 K at doses ranging from 1.0×10^{15} ions/cm^2 to 1.0×10^{16} ions/cm^2. Irradiation characteristics and results for sample 82 are shown in Table 4.1, and Figure 4.2 is a plot of the product Dt versus fluence for sample 82. This analysis allows the mixing parameter to be calculated using equation 4.1. This work has calculated $\xi = 2.1 \pm 0.2$ Å$^5 eV^{-1}$, which is a low value for the mixing parameter, indicating that ion mixing is dominated by ballistic mixing and that thermal spike activity is negligible. Data for 295 K irradiations at fluence of 1.0×10^{16} ions/cm^2 for samples 86, 88, and 91 is also shown in

Figure 4.2. The points for samples 88 and 91, which are also textured, are near the best-fit line and agree with the mixing parameter found for sample 82. Sample 86 was shown to be single crystal and its measured data point does not agree with data for 82 and 88. The measured *Dt* is much lower, which would result in a much lower mixing parameter than found for sample 82.

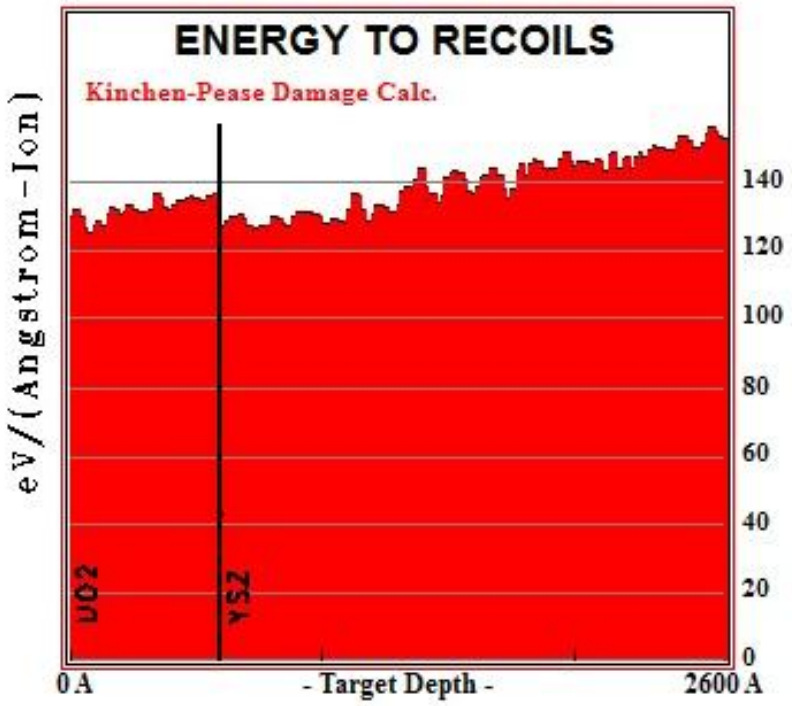

Figure 4.1: Differential energy deposition results for UO_2 irradiated with 1.8 MeV Kr^+ from TRIM calculation. The thickness of the UO2 film is set to be 600 A, which is the thickness of sample 82.

Table 4.1: Irradiation characteristics, measured standard deviations, and calculated total mean squared distances for sample 82.

T [K]	t [s]	Φ [1/Å^2]	σ [Å]	$\Delta\sigma^2$ [Å^2]	Dt [Å^2]
295	0	0	18.9 ± 0.2	0	0
295	324	0.1	19.8 ± 0.2	32.2	16.1 ± 5.3
295	324	0.1	19.6 ± 0.2	29.4	14.7 ± 5.8
295	972	0.3	22.7 ± 0.2	159.0	79.5 ± 6.5
295	1620	0.5	26.7 ± 0.2	355.7	177.9 ± 6.1
295	3240	1.0	29.5 ± 0.2	513.8	256.9 ± 8.1

$\Delta\sigma^2 = (\sigma)^2 - (\sigma_{ref})^2$
$\Delta\sigma^2$ is calculated with $\sigma_{ref} = \sigma_{unirr}$

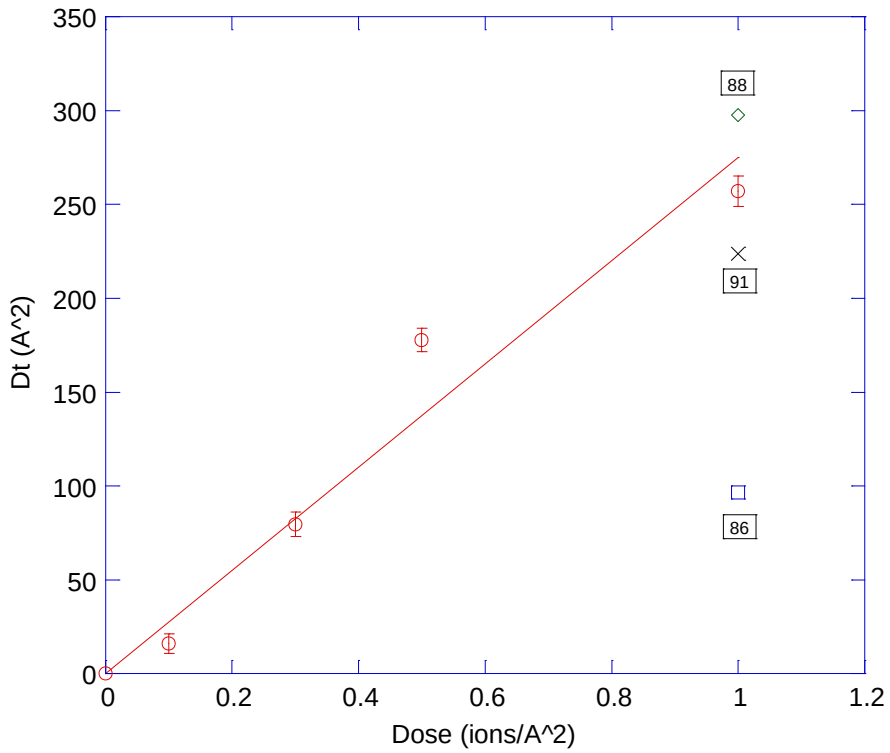

Figure 4.2: Product *Dt* (the total mean squared displacement in one-dimensional diffusion) versus fluence (in units of ions/Å^2) for heavy ion bombardment at room temperature. The best-fit line, which is forced through the origin (zero displacement at zero fluence), is proportional to the mixing parameter. Data points for samples 86, 88, and 91 are also shown.

4.2 Radiation Enhanced Diffusion

An Arrhenius plot (log D versus 1000/T) comparing samples 86 and 88 is shown in Figure 4.3. The measured radiation enhanced diffusivity D_{RED} and the measured thermal diffusivity D_T are shown. The data is fit to an Arrhenius equation the form,

$$D = D_0 exp\left(\frac{-E_a}{kT}\right) \quad (4.3)$$

where *k* is the Boltzmann's constant, E_a is the activation enthalpy, D_0 is the diffusion constant. Activation enthalpies and diffusion constants have been tabulated in Table 4.5.

Figure 4.4 is an Arrhenius plot of the thermal diffusion coefficient, comparing reported data to data measured in the present work. Reported data was performed at much greater temperatures than this work, which makes comparison to present work difficult. Table 4.6 compares reported thermal diffusion coefficients and activation enthalpies to those found in the present work.

Table 4.2: Irradiation characteristics, measured standard deviations, and calculated total mean squared distances for sample 86.

T [K]	t [s]	Φ [1/Å^2]	σ [Å]	$\Delta\sigma^2$ [Å^2]	D [$\times 10^{-18}$ cm^2/s]
295	0	0	11.6 ± 0.2	--	--
295	3240	1.0	18.1 ± 0.2	--	--
393	0	0	12.9 ± 0.1	31.2$^-$	0.41 ± 0.04
393	3240	1.0	21.7 ± 0.3	144.7$^+$	1.9 ± 0.09
473	0	0	13.8 ± 0.2	55.2$^-$	0.85 ± 0.05
473	3240	1.0	34.6 ± 0.3	869.2$^+$	13.4 ± 0.2
573	0	0	18.0 ± 0.2	191.3$^-$	2.6 ± 0.06
573	3240	1.0	68.3 ± 0.9	4340.4$^+$	58.8 ± 0.8
623	3240	1.0	86.1 ± 1.3	7092.8$^+$	96.1 ± 1.5

$\Delta\sigma^2 = (\sigma)^2 - (\sigma_{ref})^2$

$^-$ $\Delta\sigma^2$ is calculated with $\sigma_{ref} = \sigma_{unirr}$

$^+$ $\Delta\sigma^2$ is calculated with $\sigma_{ref} = \sigma_{RT}$

Table 4.3: Irradiation characteristics, measured standard deviations, and calculated total mean squared distances for sample 88a and 88b.

T [K]	t [s]	Φ [1/Å^2]	σ [Å]	$\Delta\sigma^2$ [Å^2]	D [$\times 10^{-18}$ cm^2/s]
295*	0	0	12.9 ± 0.2	--	--
295**	0	0	11.7 ± 0.4	--	--
295*	3240	1.0	27.6 ± 1.1	--	--
393*	0	0	16.3 ± 0.6	99.2$^-$	1.5 ± 0.2
393*	3240	1.0	43.4 ± 1.8	1118.9$^+$	17.3 ± 1.3
473*	0	0	22.5 ± 1.0	343.2$^-$	5.3 ± 0.2
473*	3240	1.0	57.8 ± 1.6	2575.2$^+$	39.7 ± 1.5
573**	0	0	31.1 ± 1.6	804.4$^-$	12.4 ± 0.7
573**	3240	1.0	75.0 ± 2.9	4859.2$^+$	75.0 ± 3.4
623**	3240	1.0	85.7 ± 3.4	6580.8	101.6 ± 4.5

* Sample 88a
** Sample 88b

$\Delta\sigma^2 = (\sigma)^2 - (\sigma_{ref})^2$
$^-$ $\Delta\sigma^2$ is calculated with $\sigma_{ref} = \sigma_{unirr}$
$^+$ $\Delta\sigma^2$ is calculated with $\sigma_{ref} = \sigma_{RT}$

Table 4.4: Irradiation characteristics, measured standard deviations, and calculated total mean squared distances for sample 91.

T [K]	t [s]	Φ [1/Å^2]	σ [Å]	$\Delta\sigma^2$ [Å^2]	D [$\times 10^{-18}$ cm^2/s]
295	0	0	13.3 ± 0.4	--	--
295	3240	1.0	25.0 ± 0.4	--	--
393	3240	1.0	40.6 ± 1.1	1026.4$^-$	15.8 ± 0.07
473	0	0	21.5 ± 0.2	284.7$^+$	4.4 ± 0.1

$\Delta\sigma^2 = (\sigma)^2 - (\sigma_{ref})^2$

$^-$ $\Delta\sigma^2$ is calculated with $\sigma_{ref} = \sigma_{unirr}$

$^+$ $\Delta\sigma^2$ is calculated with $\sigma_{ref} = \sigma_{RT}$

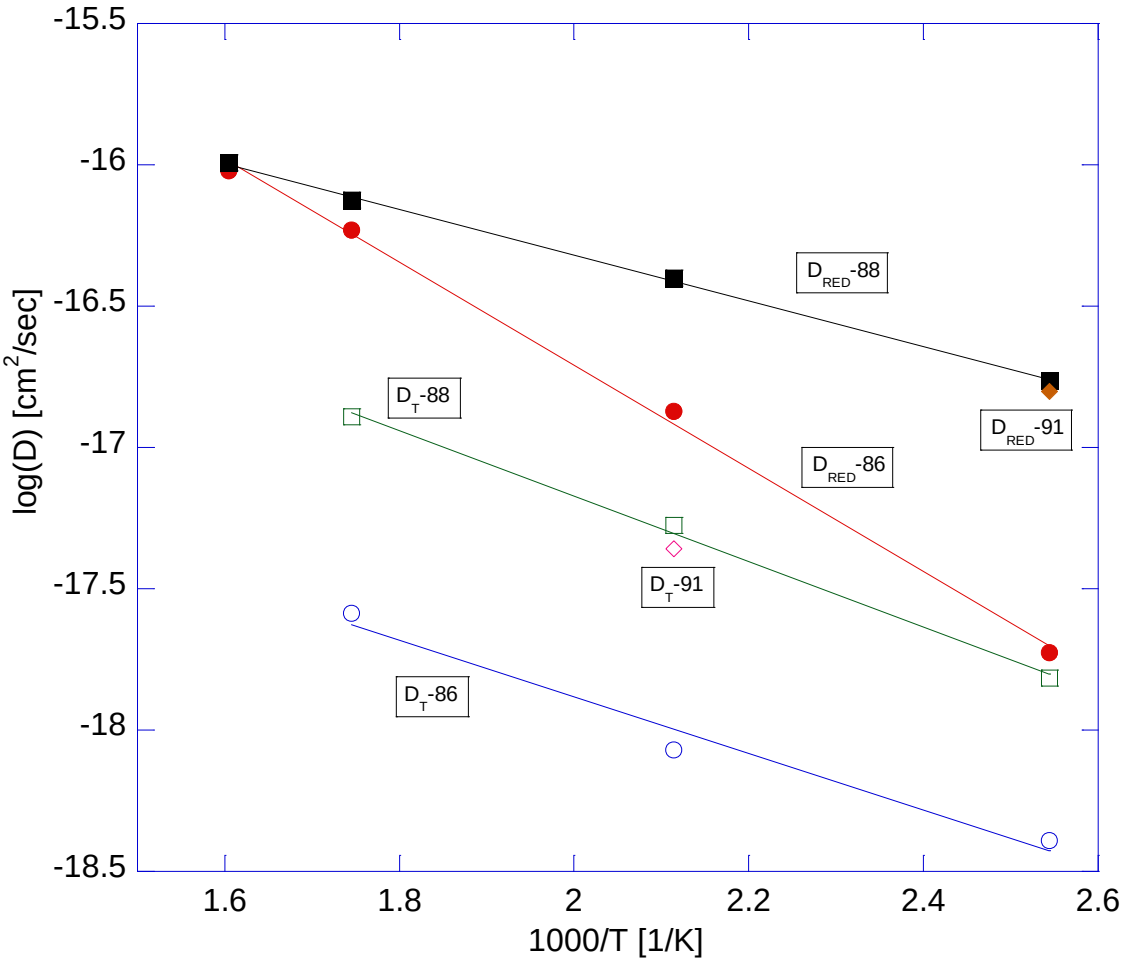

Figure 4.3: Arrhenius plot of the measured radiation enhanced diffusion coefficient and the thermal enhanced diffusion coefficient for samples 86, 88, and 91 at elevated temperature during heavy-ion bombardment.

Table 4.5: Measured diffusion coefficients and activation enthalpies.

Sample		D_0 [cm^2/sec]	E_a [eV]
86	D_{RED}	8.7×10^{-14}	0.83
	D_T	1.3×10^{-16}	0.46
88	D_{RED}	2.0×10^{-15}	0.37
	D_T	1.4×10^{-15}	0.53

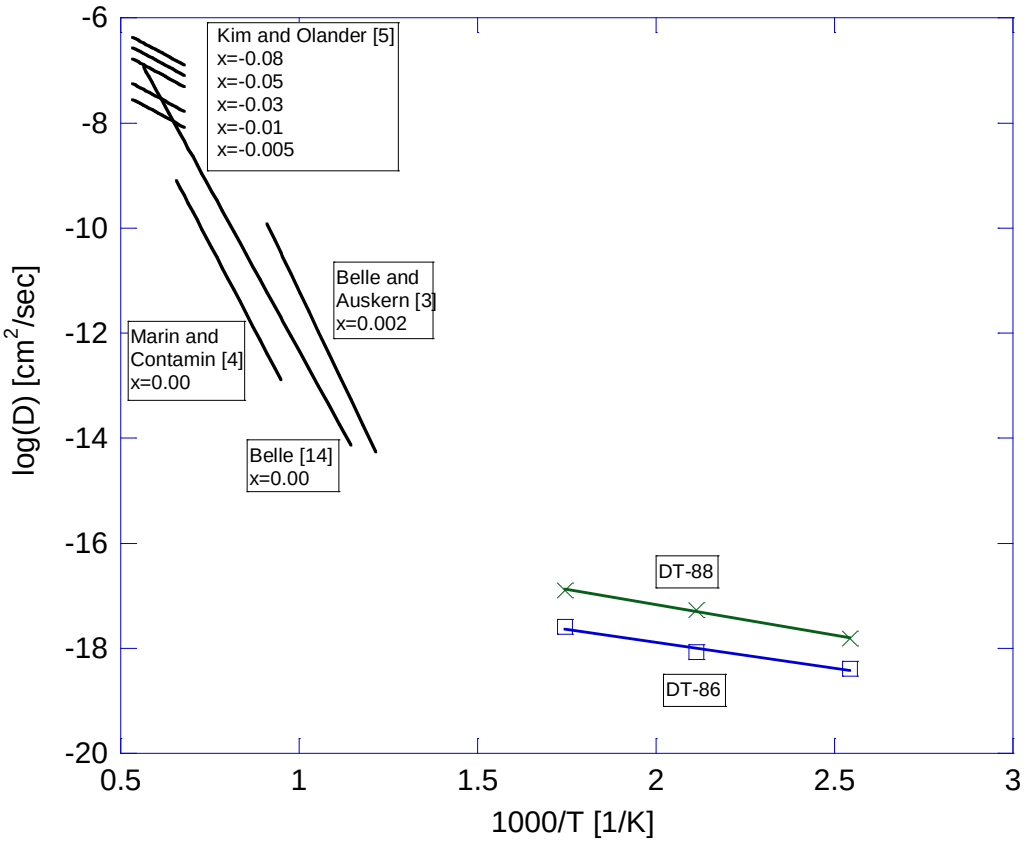

Figure 4.4: Arrhenius plot of the thermal diffusion coefficient of oxygen in UO_2, comparing reported data to data measured in the present work. Reported data was performed at much greater temperatures, which makes comparison to present work difficult.

Table 4.6: Comparison of reported and present work thermal diffusion coefficients and activation enthalpies.

Source	Structure	|x|	D_0 [cm^2/sec]	E_a [eV]
Auskern and Belle[3]	UO_{2+x}	0.002	1.20×10^{3}	2.83
		0.004	7.0×10^{-6}	1.29
		0.063	2.06×10^{-3}	1.29
Marin and Contamin[4]	$UO_{2.00}$	0.00	0.26	2.57
Belle[14]	$UO_{2.00}$	0.00	1.15	2.46
Kim and Olander[5]	UO_{2-x}	0.005	0.11×10^{-5}	0.507
		0.01	0.22×10^{-5}	0.507
		0.03	0.65×10^{-5}	0.507
		0.05	1.07×10^{-5}	0.507
		0.08	1.68×10^{-5}	0.507
Dorado *et al.*[15]	$UO_{2.00}$	0.00	--	3.2
Present Work	Sample 86	--	1.3×10^{-16}	0.46
	Sample 88	--	1.4×10^{-15}	0.53

CHAPTER 5: DISCUSSION

Anion thermal diffusion and radiation enhanced diffusion (RED) measurements have been made for both single crystal and textured UO_2 thin films. Sample 86 was single crystal, while samples 88 and 91 were textured. This difference in crystal structure led to significantly different results. Differences in stoichiometry could have contributed to these differences, as well. Sample 91 was used to reproduce the diffusion measurements for 88, a textured film. The activation enthalpy and diffusion coefficient were shown to agree for each textured sample. Unfortunately, the same reproduction was not able to be done for sample 88, since another single crystal film was unable to be grown. The growth procedure used for sample 86 was reproduced but yielded textured films. However, sample 86 was grown after the magnetron sputtering chamber had been cleaned. The chamber would have been rid of various impurities that are generally found in the sputtering chamber, which could have promoted single crystal growth. This cleaning process is not repeated after each growth because it requires significant downtime and extensive cleaning.

In the present work, the temperature region from 295 K to 623 K was analyzed. The temperature region was limited to 623 K for this work because of the high anion diffusivity in UO_2 at elevated temperatures. At higher temperatures, the ^{18}O peak would interact with the surface and the film/substrate interface, which would lead to incorrect results. Thermal diffusion measurements were made for both the single crystal and the textured films. The diffusion constant for sample 86 was shown to be a factor of 10 smaller than for sample 88 and 91. In the UO_{2+x} system the diffusion constant is strongly dependent on x. Kim and Olander made a series of measurements on the UO_{2-x} anion sublattice for a number of different values of x. When x was varied from -0.005 to -0.05, the diffusion constant increased by a factor of 10 [5]. This shows that relatively small deviations in x can have a large impact on the diffusion constant. In this

work, the value of x is unable to be measured. However, it is quite possible that the stoichiometry is slightly varied between sample 86 and samples 88 and 91, which could lead to the differences seen in the diffusion *constant*. The anion diffusion coefficient increases with increasing deviations from stoichiometry, which leads to the conclusion that the absolute value of x is larger in the textured samples than in the single crystal film. Another potential cause of this difference is the entropy term in the diffusion coefficient. Grain boundaries in the textured films, not seen in the single crystal film, would facilitate vacancy formation and increase entropy in the film. The diffusion constants measured in this work are well below published values for anion diffusion. This difference is illustrated in Figure 4.4. However, present work was conducted at much lower temperatures. This leads us to believe that there is a transition of diffusion regimes between the low temperatures measured in the current work and the high temperatures measured in published work. This transition could possibly be due to a change in the diffusing species; from vacancy controlled diffusion to interstitial controlled diffusion.

Matzke studied the anion diffusion processes in UO_2 and produced experimental and calculated formation, migration, and Arrhenius activation energies of oxygen in the UO_2, UO_{2+x}, and UO_{2-x} systems, which can be seen in Table 5.1 [2]. For UO_{2+x}, anion interstitials are the dominant diffusion mechanism, while for UO_{2-x}, anion vacancies are the dominant diffusion mechanism. This is clearly shown in Table 5.1, which shows that the activation energy for UO_{2+x} is equal to the oxygen interstitial migration energy and the activation energy for UO_{2-x} is equal to the oxygen vacancy migration energy. The activation enthalpies found in this work, from best fit analysis, are similar for both the single crystal and textured films. Activation enthalpies were determined to be $E_a = 0.46 \pm 0.08$ for sample 86 and $E_a = 0.53 \pm 0.03$ for sample 88. These results are similar to predicted Arrhenius activation energies for anion vacancies and are on the

lower end of the experimental values and equal to the calculated value for the UO_{2-x} system for anion vacancies. Kim and Olander also measured activation energy of E_a = 0.51 eV for the UO_{2-x} system [5]. Although it is difficult to say with certainty, it is likely that films used in this work are substoichiometric. This would lead to the diffusion in these films being controlled by vacancies in UO_{2-x}.

Diffusion processes under heavy-ion bombardment can be simplified into two different kinetic regimes, namely recombination-limited kinetics and sink-limited kinetics. At low temperatures and low sink concentrations, the recombination of vacancies and interstitials is the dominant kinetics mechanism, while the loss of point defects to sinks is low. In an Arrhenius plot, this will be indicated by a linear increase in D_{RED} with increasing temperature. In this regime, the migration enthalpy is two times that of the measured activation enthalpy,

$$E_a = \frac{1}{2} E_m \quad (5.1)$$

where E_m is the point defect migration enthalpy. At high temperatures or high sink concentrations, sink-limited kinetics is the dominant mechanism. Point defects annihilate at sinks. D_{RED} is independent of temperature in this regime because fixed sink concentrations do not vary with temperature and the diffusion length is fixed.

Radiation enhanced diffusion measurements were also performed from 295 K to 623 K for both the single crystal and textured films. In this temperature region, there was a linear dependence of D_{RED} on temperature, which is shown in Figure 4.3. This linear dependence of D_{RED} on temperature is therefore characteristic of a recombination-limited kinetics regime. The activation enthalpies found from best fit analysis are E_a = 0.83 ± 0.06 for sample 86 and E_a = 0.37 ± 0.02 for sample 88. The activation enthalpies on the anion sublattice are approximately twice as large for the single crystal film as that of the textured films. The decrease

in activation energy from the single crystal film to the textured films is expected. These textured films have a greater dislocation density and a greater sink concentration, which will result in a decrease in the activation energy. The shift from recombination-limited kinetics to sink-limited kinetics occurs at lower temperatures when higher sink concentrations are greater. This transition will occur at lower temperatures for samples 88 and 91 than for sample 86. As the sink density continues to increase the radiation enhanced diffusion coefficient will become athermal. If we assume that we are in a region of recombination-limited kinetics, from equation 5.1, the corresponding migration enthalpy is E_m = 1.66 ± 0.12 for sample 86 and E_m = 0.74 ± 0.04 for sample 88. However, the migration energies for RED should not be larger than the activation energies seen in the thermal case. In the thermal case, the activation energy is equal to the sum of the migration and formation energies, while for RED, heavy-ion bombardment provides the energy necessary to form Frenkel pairs. Therefore, the activation energies seen for RED must be influenced by other factors. The conclusion cannot be made that diffusion is dominated by recombination of vacancies and interstitials, since the migration energies calculated appear to be unphysical.

To calculate the mixing parameter ξ, room temperature irradiations were done at doses ranging from 1.0×10^{15} ions/cm^2 to 1.0×10^{16} ions/cm^2. The mixing parameter characterizes diffusivity associated with displacement cascades, and directly shows the effects of the type of irradiation particle, specimen temperature, and ion flux [7, 12]. At 303 K, transport calculations predict ξ to be 2-5 $\text{Å}^5 eV^{-1}$ for the anion sublattice, which is indicative of ballistic mixing and relatively independent of the material [12]. Figure 4.2 displays mixing parameter data for sample 82 (data points for samples 86, 88, and 91 are also shown). This work has calculated $\underline{\xi}$ = 2.1 ± 0.2 $\text{Å}^5 eV^{-1}$, which falls into the range predicted above. This analysis displays a low

mixing parameter, indicating that ion mixing is dominated by ballistic mixing and that thermal spike activity is negligible. Low values are generally taken to be values less than 5 $\text{Å}^5 eV^{-1}$. Thermal-spike mixing refers to the local atomic transport that may occur when a crystal lattice is heated locally after the ballistic phase of a displacement cascade [21]. The high melting temperature of UO_2 (3140 K) will reduce the atomic transport during thermal-spike mixing, which leads to a low value of the mixing parameter.

Table 5.1: Experimental and calculated migration, formation, and activation energies of oxygen in UO_2 [2].

		Experimental	Calculated
Formation energies (eV)	O-Frenkel Pair	3.0-4.0	4.8
Migration energies (eV)	O-vacancy	0.5-0.7	0.5
	O-interstitial	0.8-1.0	0.6
Arrehenius activation energies (eV)	UO_{2+x}	0.8-1.0	0.6
	UO_2	2.6	2.8
	UO_{2-x}	0.5-0.7	0.5

CHAPTER 6: SUMMARY

Anion radiation enhanced diffusion (RED) and thermal diffusion of a buried ^{18}O tracer layer in thin film UO_2 was measured using Secondary-Ion Mass Spectroscopy (SIMS). UO_2 thin films were grown using a dedicated magnetron sputtering chamber. Thin films were grown at 295 K on YSZ substrates. Samples were characterized using XRD, XRR, XPS, and SIMS. Single crystal and textured thin films were studied in this analysis. These samples were then irradiated with 1.8 MeV Kr^+ over a temperature range from 295 K to 623 K. The difference in crystal structure between single crystal and textured thin films was shown to significantly affect RED and thermal diffusion results. Thin film stoichiometry was also thought to have a significant effect on RED and thermal diffusion. For RED, the single crystal activation enthalpy E_a = 0.83 was significantly larger than the activation energy E_a = 0.37 for textured films. RED for single crystal UO_2 thin films can be represented by,

$$D_{RED} = 8.7 \times 10^{-14} \exp\left(\frac{-0.83}{\mathrm{kT}}\right) cm^2/sec$$

RED for textured UO_2 thin films can be represented by,

$$D_{RED} = 2.0 \times 10^{-15} \exp\left(\frac{-0.37}{\mathrm{kT}}\right) cm^2/sec$$

Thermal diffusion measurements were also performed for the same samples. Half of each sample, used for irradiation at elevated temperature, was not placed in the path of the beam. This allowed each half of the sample to be exposed to the same thermal history. Thermal diffusion measurements resulted in similar activation enthalpies, E_a = 0.46 for single crystal films and E_a = 0.53 for textured films. These activation enthalpies were shown to agree well with published experimental and calculated values for UO_{2-x} for anion vacancies by Matzke and Kim

and Olander [2, 5]. Thin films used in this work were thought to be substoichiometric and thermal diffusion is thought to be controlled by anion vacancies.

Irradiations were performed at 295 K to determine a mixing parameter. Mixing parameter measurements found $\xi = 2.1 \pm 0.2$ $\text{Å}^5 eV^{-1}$, which was consistent with previous results on the anion sublattice. This analysis displays a low mixing parameter, indicating that ion mixing is dominated by ballistic mixing and that thermal spike activity is negligible.

CHAPTER 7: FUTURE WORK

Because of the complexities of thin films and thin film growth, obtaining quality films to use in this work was difficult. Radiation enhanced diffusion measurements are complicated, and stoichiometry and specimen uniformity can have a large impact on RED measurements. Films used in this work were single crystal and textured, which were shown to yield differing results. In future work, the growth process should be controlled to yield films with consistent uniformity and stoichiometry. Because of the size of the YSZ substrates used, films could be grown on multiple substrates during the same growth. This would ensure consistency and would allow for measurements to be performed on a wider range of temperatures with one sample growth. For future work, it would also be useful to solely use single crystal films in analysis. If single crystal films were used, RED measurements could be done without the possibility of grain boundaries effecting diffusion. Obtaining exact stoichiometry of thin films is difficult. However, determining the exact stoichiometry of these samples would allow for a comparison of measured data to expected values published in literature. Additionally, because stoichiometry greatly affects RED measurements, it would be very beneficial to know the stoichiometry of films.

Published work has been conducted at much higher temperatures than the temperature regime studied in this analysis. This difference in temperatures makes comparison of the results difficult. The diffusion constants measured in this work are well below published values for anion diffusion. This significant difference in diffusion constants between temperature regimes would make two additional temperature regimes useful to analyze. The regime from 623 K to 823 K could be analyzed to measure diffusion properties of ^{18}O in UO_2 to determine a potential transition region between this work and published work. The regime from 823 K to 1873 K could be analyzed to compare diffusion properties of ^{18}O in UO_2 thin films to that of bulk

material used in published work. In order to perform measurements in these regimes, it would be necessary to use samples with a greater film thickness. This would allow for the greater diffusion expected on the anion sublattice. Future measurements at elevated temperatures would also be more applicable to reactor conditions.

BIBLIOGRAPHY

[1] J. Janek and H. Timm, J. Nucl. Mat. 225 (1998) 116.

[2] Hj. Matzke, J. Less-Common Metals 121 (1986) 537.

[3] A. B. Auskern and J. Belle, J. Nucl. Mat. 3 (1961) 311.

[4] J. E. Marin and P. Contamin, J. Nucl. Mat. 30 (1969 16.

[5] K.C. Kim and D.R. Olander, J. Nucl. Mat. 102 (1981) 192.

[6] A. HÖH, Hj. Matzke, J. Nucl. Mat. 48 (1973) 157.

[7] H. K. Pappas, B. J. Heuser, M. M. Strehle, J. Nucl. Mat. 405 (2010) 118.

[8] R. Sizmann, J. Nucl. Mater. 69-70 (1968) 386.

[9] G.J. Dienes, A.C. Damask, J. Appl. Phys. 29 (1958) 1713.

[10] W. M. Lomer, United Kingdom Atomic Energy Administration Report AERE-T/R 1540 (1954).

[11] P. G. Shewmon, Diffusion in Solids (McGraw-Hill, New York, 1963).

[12] A. I. Sambeek, *et al.*, J. Appl. Phys. **83** (1998) 7576.

[13] G.E. Murch, C. Richard, and A. Catlow, J. Chem. Soc., Faraday Trans. 2 83 (1987) 1157.

[14] J. Belle, J. Nucl. Mat. 30 (1969) 3.

[15] B. Dorado, *et al*., J. Nucl. Mat. 400 (2010) 103.

[16] F. Gupta, *et al*., Phil. Mag. 87 (2007) 2561.

[17] G. Martin, *et al.*, J. Nucl. Mat. 385 (2009) 351.

[18] M. M. Strehle, *et al.*, Thin Solid Films 520 (2012) 17.

[19] R. G. Wilson, F. A. Stevie, C. W. Magee, *Secondary Ion Mass Spectroscopy*. New York: Wiley, 1989, pp. 1.3-1 - 1.3-2.

[20] H. Idriss, Surf. Sci. Rep. 65 (2010) 67.

[21] S.-J. Kim, M.-A. Nicolet, R. S. Averback, D. Peak, Phys. Rev. B 37 (1988) 38.